



Unsaturated permeability of clayey soil during desiccation: combined evaporation-shrinkage-cracking

Fatma Louati¹ · Houcem Trabelsi¹ · Yahya Alassaf² · Mehrez Jamei² · Said Taibi³

Received: 18 December 2021 / Accepted: 2 April 2023 / Published online: 23 May 2023
© Springer-Verlag GmbH Germany, part of Springer Nature 2023

Abstract

Desiccation cracking significantly affects the unsaturated permeability (K_{unsat}), which governs the water diffusion in the soil in several engineering applications, such as slope stability, road embankments, long-term risk assessment from waste disposal sites, recharge for groundwater hydrogeology, petroleum, and CO₂ storage. Cracking causes the permeability to increase, which is cited as the cause of failure and damage in a number of the aforementioned works. This paper aims to experimentally study the unsaturated permeability (K_{unsat}) of a clayey soil during desiccation. Similar to the instantaneous profile method (IPM), a new method was developed that is based on evaporation tests and water retention curve (SWRC) and takes into account the strains caused by shrinkage and cracks. Different initial states of a clayey soil are examined including a slurry soil prepared at the liquid limit water content and compacted soil with varying initial densities on the wet part on the normal optimum proctor (NPO). Two additional image methods were used: the DIC technique (digital image correlation) to investigate the strain field before cracking and the IAT (image analysis technique) to study the growth of cracks. It was demonstrated that K_{unsat} was well related to the initial state in terms of density and moisture content. When the suction reaches the entry suction value, K_{unsat} decreases when the suction increases without the appearance of desiccation cracks. Otherwise, it increases with the growing intensity of the cracks. The proposed experience protocol allowed for different initial states (density and water content) to be considered in a large suction range without the use of proximity sensors.

Keywords Clayey soil · Initial density · Initial moisture content · Water retention curve · Desiccation cracks · Evaporation · Unsaturated permeability

Introduction

Although unsaturated permeability is the primary parameter that governs the hydraulic behavior of clayey soils during drying, the vast majority of the geotechnical works in the literature deal with the saturated state using exclusively saturated permeability (Louati et al. 2018a; Xu et al. 2020).

During drying, the water content of soils decreases and suction increases, which results in an increase in tensile strength and then a network growth of cracks (Lakshmikantha et al. 2009; Trabelsi et al. 2012). The importance of cracks in clayey soil has motivated scientists to study the propagation of desiccation cracks under different boundary conditions (Hallett and Newson 2001; Tang et al. 2011; Wei et al. 2020, 2021). Desiccation significantly increases the water infiltration content; however, the experimental understanding of the hydrological consequences of cracks and volume changes in permeability is still limited. Consequently, this study aims to determine the permeability during desiccation based on evaporation tests as well as the water retention property and takes into account the variation of volume change and cracks.

Primarily, the evaporation rate has been recognized to play an important role in crack initiation and propagation (Costa et al. 2013), while the water characteristic curve (WRC) is the key parameter for determining unsaturated

✉ Mehrez Jamei
mehjamei@yahoo.fr; mehrez.jamei@nbu.edu.sa

¹ Laboratory of Civil Engineering, National Engineering School of Tunis, University of Tunis El Manar, B.P. 37, 1002 Belvedere, Tunis, Tunisia

² Civil Engineering Department, Northern Border University, Engineering College, Arar, Saudi Arabia

³ Laboratory of Waves and Complex Media, UMR 6294, CNRS, University of Le Havre Normandy, 53, Rue Prony, BP 540, 76058 Le Havre, France

permeability during desiccation. Soils' WRC depends on several factors, such as soil structure (Vanapalli et al. 1999), soil type (Miller et al. 2003; Marinho 2005), and temperature (Romero et al. 2001; Zhou et al. 2014). For the same type of soil, the effect of stress states on the WRC can be attributed to the density change effect. Sun et al. (2007) and Sun et al. (2016) have reported that the WRC mainly depends on density rather than the stress state. These studies investigated the density effect on the WRC (Romero et al. 1999; Birle et al. 2008; Salager et al. 2013). However, only a few studies have investigated the effect of density on the unsaturated permeability of compacted clayey soil during desiccation. Accordingly, it is crucial to determine the permeability of clayey soil, taking into account the effect of initial density and soil structure variation during drying. Wang et al. (2013) proposed a statistical method based on the automatic generation of a 3D crack network, which was used to predict the anisotropic permeability of saturated, cracked soil.

As indicated in the literature, the effects of density on soil structure have been investigated by several authors (Blackwell et al. 1986; Horn et al. 1995; McNabb et al. 2001). Other studies, such as that of Romero et al. (1999), attempt to shed more light on the relationship between the microstructure of their sample and its water retention behavior. In the above-referred study, the authors carried out their experiments on a moderately swelling clay (20–30% kaolinite, 20–30% illite, and 10–20% smectite) with a liquid limit of $w_L = 56\%$, a plastic limit of $w_p = 29\%$, and 50% of particles < 2 mm. They concluded that, for a water content above 15%, the WRC depends on the void ratio in the wetting–drying paths. They added that the increase in the soil dry density results in an increase in the air entry value. However, it is reported that the WRC does not depend on the soil dry density for a water content ranging from 5 to 15%. Further, it is noted that for dry soils, that is, when the water content is less than 5%, the drying and wetting paths converge. It can, therefore, be concluded that the soil water retention behavior is governed by the microstructure, mainly by the water present in the inter-aggregate pores during the initial compaction.

During desiccation, the cracks play a decisive role in the clayey soil hydraulic behavior (Julina and Thyagaraj 2020; Cheng et al. 2020). While the variation of permeability was investigated, the explanation should be confirmed by the microstructure and macrostructure analyses. Trabelsi et al. (2018) studied the role of the fabric–soil structure on both the water retention porosity and the tensile strength. Permeability is strongly affected not only by void ratio but also by pore structure (Wang et al. 2019; Li et al. 2021). In fact, for deformable soils, there is a significant variation in the pore structure. In this paper, a desiccation test was carried out on a clayey soil, and the volume change, cracks, and porosity were determined.

So far, the instantaneous profile method (IPM) has been used to measure the unsaturated permeability but is not suitable for cracked clayey soil due to some limitations: Firstly, permeability measurement depends on the spacing of sensors. If the number of sensors was increased, it would lead to a cost increase and may cause sample damage. Secondly, the suction measurement limit is about 100 kPa for the tensiometers (Fujimaki and Inoue 2003; Schindler et al. 2015; Louati et al. 2018b, 2021). Thirdly, during desiccation, the water content decreases and cracks appear, resulting in poor contact between the specimen and the sensors. Such a problem needs to be solved in the permeability tests. Gueddouda et al. (2016) developed an experimental technique used for determining the unsaturated permeability in desiccators. However, the test is very long and time-consuming. In addition, the sample is not thick enough (1 cm), and the desiccation cracks cannot be represented. To the best of the authors' knowledge, a suitable experimental method for the determination of unsaturated permeability for a cracked clayey soil during desiccation has never been achieved. The aforementioned literature analyzes permeability in a nondeformable soil without taking into account the change in pore structure during desiccation. Besides, permeability cannot be easily determined in a large suction range. The present study is aimed at bridging this gap by investigating the unsaturated permeability of a clayey soil with different initial states in a large suction range, taking into account both volume change and the appearance of cracks and their evolution during the desiccation process using a new method derived from the IPM.

Different techniques have been developed in the literature to study the initiation and propagation of cracks in fine soils. Among these, the digital image correlation (DIC) technique during desiccation kinetics, complemented by a binary image analysis after cracking, is the most widely used (Hattab et al. 2020; Wei et al. 2021; El hajjar et al. 2021).

In this paper, the WRCs of slurry and compacted specimens were determined with different initial densities. At the macroscopic level, the strain tensors of the clays during drying, as well as the cracking phenomenon, were studied using the digital image correlation technique. After that, the corresponding soil hydraulic properties (saturated and unsaturated permeability) were measured, leading to a more likely and better understanding of the hydraulic behavior of cracked clay. This experimental study was conducted according to the following steps: (1) First, a series of samples were prepared at initial dry density (γ_d) and moisture content (w) by static compaction. (2) The WRCs were determined based on the initial state of samples (γ_d, w) and were then submitted to drying and wetting paths to demonstrate the hydraulic hysteresis behavior. However, only the dried path was considered for suction determination. (3) Using the evaporation profile method, the suction gradient and rate of water evaporation

Table 1 Beja clay physical and chemical properties

Soil properties	Value
Solids density	2.70 Mg/m ³
Liquid limit	67%
Plastic limit	28%
Shrinkage limit (for slurry)	Around 15%
Plasticity index	39%
Fraction of fines (< 80 μm)	97%
Clay-size fraction (< 2 μm)	16%
Soil organic content	0.72%
Calcium carbonate content (AFNOR NF X31-106)	36.8%
Clay minerals (qualitative XRD)	
Smectite	62%
Illite	22%
Kaolinite	16%
Chemical constituents and LOI at 800 °C	
SiO ₂	33.72%
CaO	33.62%
Al ₂ O ₃	4.38%
Fe ₂ O ₃	3.04%
K ₂ O	0.65%
TiO ₂	0.56%
Na ₂ O	0.20%
MgO	0.03%
LOI	23.78%

were determined without placing sensors inside the cracked samples. Using WRC as a noninvasive (nondestructive) method, the moisture content was measured to obtain suction. Considering the shrinkage, the variation in height of the sample during the drying test was quantified by the image analysis technique using a lateral picture, taken automatically at the same time as a surface picture, and then the height was reconsidered in the hydraulic gradient calculation.

Materials and methods

Used materials

The used soil is a clay from Thibar (Tunisia), which has a liquid limit of 67%, a plastic limit of 28%, a plasticity index of 39%, and a specific gravity of 2.7. The clay mineralogy composition determined using the X-ray diffraction test is given in Table 1. Figure 1 shows the particle size distribution of Thibar clay. It can be seen that the soil consists of 16% clay fraction (< 2 μm) and about 97% fines (< 80 μm). According to the LPC-USCS classification, the soil is plastic clay (CH).

Methods

The unsaturated permeability determination depends on two steps. Two experiments were conducted with the same initial conditions (γ_d , w). The first step was the drying process that allowed the characterization of the water retention curve. The second was the evaporation test using image analysis. The sample strain field was determined by a digital image correlation technique using the VIC-2D software, and the crack evolution was analyzed using the ImageJ software. The testing conditions for compacted and slurry samples are displayed in Table 2.

Experimental determination of the water retention curve

In order to identify the unsaturated permeability, the first step is to study the drying-wetting paths to show the behavior of the clayey soil in different initial conditions. To achieve this, we determined the relationship between void ratio, water content, degree of saturation, and suction.

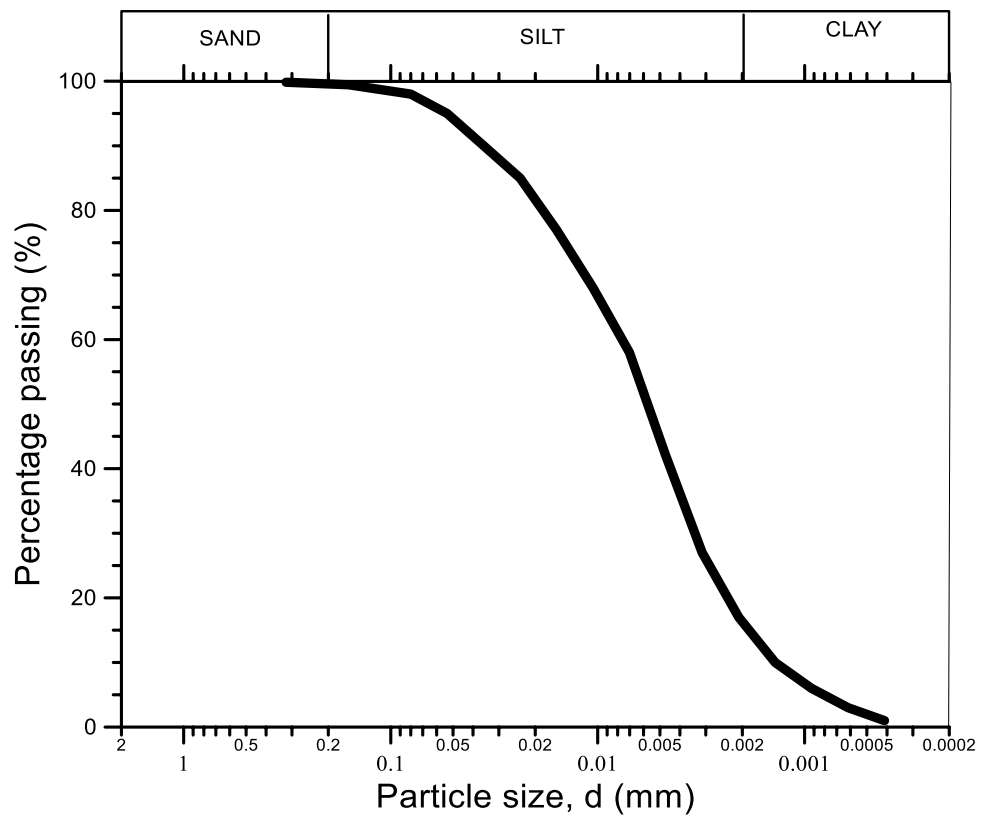
Three methods were used for determining suction during desiccation (Fleureau et al. 1993).

For $s < 20$ kPa, the samples were placed on tensiometric plates, and suction was applied to the water; the air pressure was atmospheric.

For $50 \text{ kPa} < s < 8000 \text{ kPa}$, the osmotic technique was implemented (Delage et al. 1998; Williams and Shaykewich 1969). The sample was placed in contact with organic macromolecules in a polyethylene glycol (PEG) solution through a semi-permeable membrane, which allows only water molecules to pass.

For $s > 7000$ kPa, saturated salt solutions were used, and the water transfer occurred during the vapor phase. The different samples were placed in desiccators in a temperature-controlled room (Delage et al. 1998), and the relative humidity of the atmosphere was controlled by different salt solutions (Table 3). The clay samples reached equilibrium after about 60 days. The equilibrium between the soil samples' suction and the saturated salt solution's RH was reached when the mass change did not exceed 0.01 g in 7 days. When equilibrium was reached, the properties (water content, void ratio, and saturation degree) were measured by weighing the sample after it had been immersed in a non-wetting oil (commercial Kerdane) (Tessier 1975). Concerning the sensitivity of the technique used, we followed the Delage et al. (1998) method. The authors summarized the experimental conditions in terms of the measurement uncertainty of suction and the sensitivity of the relative humidity to temperature fluctuations during the salt solution tests.

Fig. 1 The material particle size distribution



Evaporation rate and digital image correlation analysis

Evaporation experience The drying tests were carried out on slurry and compacted clays with different initial densities: 1.2 g/cm³, 1.35 g/cm³, and 1.5 g/cm³ corresponded respectively to the compacted sample’s groups noted C1, C2, and C3. All the samples were compacted at the same water content of 26%, i.e., only the dry densities reached after static compaction differs for the three groups of samples (see Table 1).

The initial water content was approximately equal to the liquid limit for slurry samples noted in this case (S). The same dimensions were used for compacted and slurry samples: 7 cm in diameter and 2 cm in height. All of the samples were dried in the same climatic conditions (a relative humidity of 60 ± 5% and a temperature of 35 ± 1 °C). For each test, an electronic balance connected to a computer was used to

measure the weights of samples, which were recorded every 10 min. Then, the change in water content was also calculated and recorded. After that, the evaporation rates (a time derivative of water content) were measured based on weight measurements provided during desiccation. The experimental device contains the soil sample support, a hygrometer (PCE-HT110-ICA), a balance, and a digital camera (Canon 600D) (see Fig. 2). The principle of the experimental technique is to impose zero suction at the bottom of the sample and control the suction (negative pressure) at the top using the hygrometer. The suction evolution in the sample was deduced from the water retention curve. The samples were sealed laterally with aluminum paper, which offers a nonadhesive and frictionless interface with the sample. As desirable consequences, neither shrinkage nor the desiccation process is impacted by aluminum paper. Evidently, the

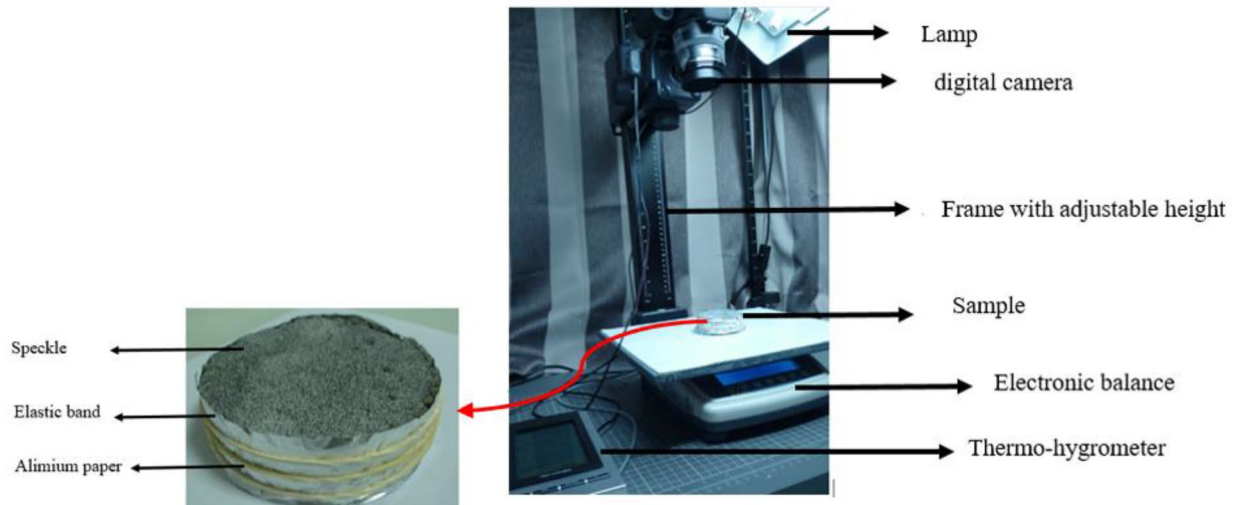
Table 2 Initial conditions of the clayey soil (S: slurry; C: compacted)

Series	Initial void ratio	Initial dry density (g/cm ³)	Initial water content (%)	Initial saturation degree (%)
C1	1.25	1.2	26	57.8
C2	1	1.35	26	63.7
C3	0.8	1.5	26	86.2
S	2	0.9	73	100

Table 3 Salt solutions used to impose higher suctions than 7 MPa at T=20 °C

Saturated salt solution	RH (%)	Suction (MPa)
CuSO ₄	95	7.1
K ₂ SO ₄	90.5	13.7
KCL	82.3	26.8
NaCL	75.2	39.3
NH ₄ CL	75.0	39.7
KNCS	59.6	71.3
LiCL	15.2	259.8

(a)



(b)

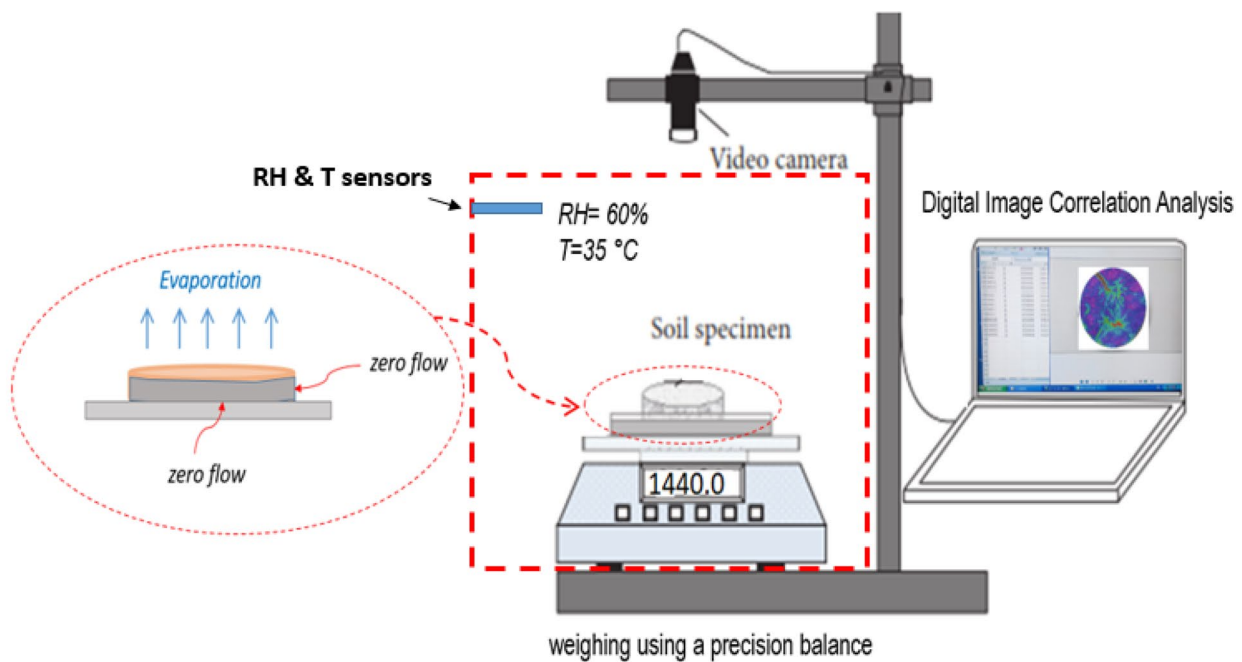


Fig. 2 Experience protocol for unsaturated permeability measurement during desiccation. **a** Experimental set-up. **b** Experimental set-up schematic

aluminum paper assures an impermeable lateral surface (no flow across this surface).

Strain field using digital image correlation analysis The sample strain was investigated using the digital image correlation (DIC) technique via the VIC-2D software that pro-

vides the strain maps (Hattab et al. 2020; El hajjar et al. 2020, 2021). During desiccation, photos of the sample surface were taken and analyzed every 10 min. For digital image correlation analyses, a random speckle pattern was obtained to allow the software to calculate the point displacements (Fig. 2a). The software analyzed the difference

in the locations of pixels between two photos and derived the displacement field and the strain map. Eid et al. (2015) explained that, using the DIC technique, the software is able to calculate the point displacements (defined from a random dot pattern or speckled pattern). During the tests, while the specimen is subjected to deformation by a constrained shrinkage, the camera takes one picture before and others after deformation, and the software analyzes the difference between the pixels of the different images and correlates them to derive the displacement as well as strain fields. Based on the VIC-2D results, the components of deformations are obtained: ε_{xx} , ε_{yy} , and ε_{xy} (in the plane defined by two axes x and y). Consequently, the major and minor principal strains ε_1 , ε_2 , and the angle (θ) of the major principal strains with respect to the x -axis are deduced as follows:

$$\varepsilon_1 = \frac{\varepsilon_{xx} + \varepsilon_{yy}}{2} + \sqrt{\left(\frac{\varepsilon_{xx} - \varepsilon_{yy}}{2}\right)^2 + (\varepsilon_{xy})^2} \quad (1)$$

$$\varepsilon_2 = \frac{\varepsilon_{xx} + \varepsilon_{yy}}{2} - \sqrt{\left(\frac{\varepsilon_{xx} - \varepsilon_{yy}}{2}\right)^2 + (\varepsilon_{xy})^2} \quad (2)$$

$$\theta = \frac{1}{2} \left(\arctan \left(\frac{2\varepsilon_{xy}}{\varepsilon_{xx} - \varepsilon_{yy}} \right) \right) \quad (3)$$

Crack evolution using ImageJ software The crack evolution was analyzed using the ImageJ software to measure the crack geometric parameters (Costa et al. 2008; Tang et al. 2008). The cracks intensity factor (CIF) is defined as the ratio between the total area of cracks and the area of the clayey sample.

Saturated and unsaturated permeability

Saturated permeability In a steady-state oedometric cell, the saturated permeability of the samples S, C1, C2, and C3 prepared according to the conditions presented in Table 2 was measured.

For the compacted soil, the samples were directly compacted in an oedometric mold of 7 cm in diameter and 2 cm in height. After placing the samples in the oedometric cell, they were saturated prior to measuring their saturated permeability in steady-state with a hydraulic gradient of $i = 6.5$.

For the slurry, the sample was directly put in the oedometric mold, and then 10 vertical progressive steps were applied. After 24 h of consolidation of each loading step, the saturated permeability was measured in steady-state with a hydraulic gradient of $i = 6.5$.

Unsaturated permeability To measure the unsaturated permeability during the desiccation test, a new method derived from IPM was developed, enabling the measurement of unsaturated permeability without the use of sensors.

The water content changed over time during the desiccation test. The unsaturated permeability was measured by investigating the change of water content, actual evaporation rate, and hydraulic gradient at elapsed times $t = t_1$ and t_2 along a 1D soil sample. The sample was laterally sealed with a thin plastic film to impose zero flow on the circumference and create a vertical one-dimensional (1D) flow condition. This plastic film does not generate any friction with the sample, does not prevent a lateral deformation of the material, and has no effect on the initiation and propagation of cracks.

The variation in water volume per unit of time is defined as the actual evaporation rate (AER) given by Eq. (4). Considering the 1D continuity equation in a vertical direction:

$$\text{AER} = \frac{\Delta m_i}{A \Delta t_i \rho_w} \quad (4)$$

where Δm_i is the sample mass difference in the time interval (kg), ρ_w is the water density (kg/m^3), A is the area of the whole sample (m^2), and $\Delta t_i = t_2 - t_1$ is the time interval (second), the total evaporated water volume of the sample (m^3) in the time interval $\Delta V_w = \Delta m_i / \rho_w$;

Then, the actual evaporation rate AER can be determined as follows, Eq. (5)

$$\text{AER} = \frac{\Delta V_w}{A \Delta t_i} \quad (5)$$

To determine the flow conditions, the Reynolds number was calculated via Eq. (6) as follows:

$$R_e = \frac{VD}{\nu} \quad (6)$$

where R_e is the flow Reynolds number, V is the water velocity (m/s), D is the hydraulic diameter (m), and ν is the water kinematic viscosity (m^2/s). Considering the viscosity value at a temperature of 30 °C (0.884×10^{-3}), the diameter D as the opening of the fissure, in the range of 0.25–1 cm, and the velocity V in the range of 0.003 – 0.92×10^{-3} m/s, the Reynolds numbers fall in the range of 4 to 260. Then the laminar flow regime has occurred, and Darcy's is valuable in the transient regime during drying.

Afterwards, the unsaturated permeability ($K_{\text{unsat}}(s)$, depending on the suction s) was measured based on Darcy's law, where i_m represents the hydraulic gradient:

$$k_{\text{unsat}} = \frac{\text{AER}}{i_m} \quad (7)$$

The evaporation experiment was carried out in the laboratory at a controlled temperature ($T=35\text{ }^\circ\text{C}$) and relative humidity ($RH=60\%$). On the upper sides of the sample, the applied suction (s) was related to the constant relative humidity (RH) and temperature (T) imposed in the climatic chamber. The suction was measured using Eq. (8), derived from Kelvin’s law:

$$s = -\rho_w \frac{RT}{M} \ln(RH) \tag{8}$$

where R is the universal gas constant, $R=8.3143\text{ J/mol K}$, T is the absolute temperature (K), M is the water molecular weight, $M=18.016\text{ g/mol}$, and RH is the relative humidity (%).

The total volume V is the sum of three-volume components: solid V_s , pore V_p , and crack V_c volumes. The solid volume corresponds to the solid mass M_s divided by the solid density ρ_s .

The void ratio (e) and the corresponding degree of saturation (Sr) of the clayey sample can be calculated from Eqs. (9) and (10). By determining the CIF and considering the crack depth as constant reaching the bottom of the sample, we can determine the volume of cracks (V_c), which is determined as the product between the area of cracks (evaluated by ImageJ analysis) and the depth (thickness of the sample). In fact, in this proposed experimental study, it was observed that the chosen dimensions of the sample favor the propagation of cracks to completely reach the bottom. For thin samples, it has been demonstrated that almost all cracks reach the bottom of the samples (see, for example, Peron et al. 2009; Tang et al. 2011; Julina and Thyagaraj 2019; Groisman and Kaplan 1994). At a given time, the total volume of the sample tested is the sum of three volumes: the V_s , V_p , and V_c volumes. In fact, the solid volume is calculated by dividing the solid mass (m_s) by the solid bulk density (ρ_s) measured using the lab glass-specific gravity bottle pycnometer device. The pore volume corresponds to the voids in the soil mass corresponding to the sample before cracking and precisely for free shrinkage, that is, without cracking (Trabelsi et al. 2018).

$$e = \frac{V_v}{V_s} = \frac{V_p + V_c}{V_s} \tag{9}$$

$$Sr = \frac{w.e}{G_s} \tag{10}$$

With $G_s = \rho_s/\rho_w$ (11)

The water ratio distribution and void ratio are the basic parameters for the measurement of the saturation degree during the desiccation test. The suction variation was calculated using the water retention curves (w , s and Sr , s) (Fig. 3a, b).

The mean hydraulic gradient (i_m) was calculated using Eq. (12), which is formulated based on the instantaneous profile method.

In fact, the hydraulic gradient was calculated, using a method similar to the instantaneous profile method, as the change in average suction. In fact, the gradient of negative water pressure (suction) was calculated as the average value between two gradients obtained, respectively, considering the water flow between the medium and bottom of the sample and then between the medium and top. To avoid palcing a sensor in damaged specimen by cracking, the suction at the medium was obtained according to the succeeding steps: (1) calculation of the void ratio considering the shrinkage, (2) calculation of the degree of saturation, and (3) using the water retention curve (WRC: suction-degree of saturation curve), we have deduced the suction.

This average suction gradient was divided by the sample height (h) which was obtained considering its variation under shrinkage, and ρ_w (9.81 kN/m3). Thus, we have obtained a dimensionless hydraulic gradient.

As it is mentioned above, average suction was calculated by measuring water content and the associated WRC for the four samples (C1, C2, C3, and S).

$$i_m = \frac{1}{2\rho_w} \left(\frac{s_s - s_{it_1}}{\Delta z} + \frac{s_s - s_{it_2}}{\Delta z} \right) \tag{12}$$

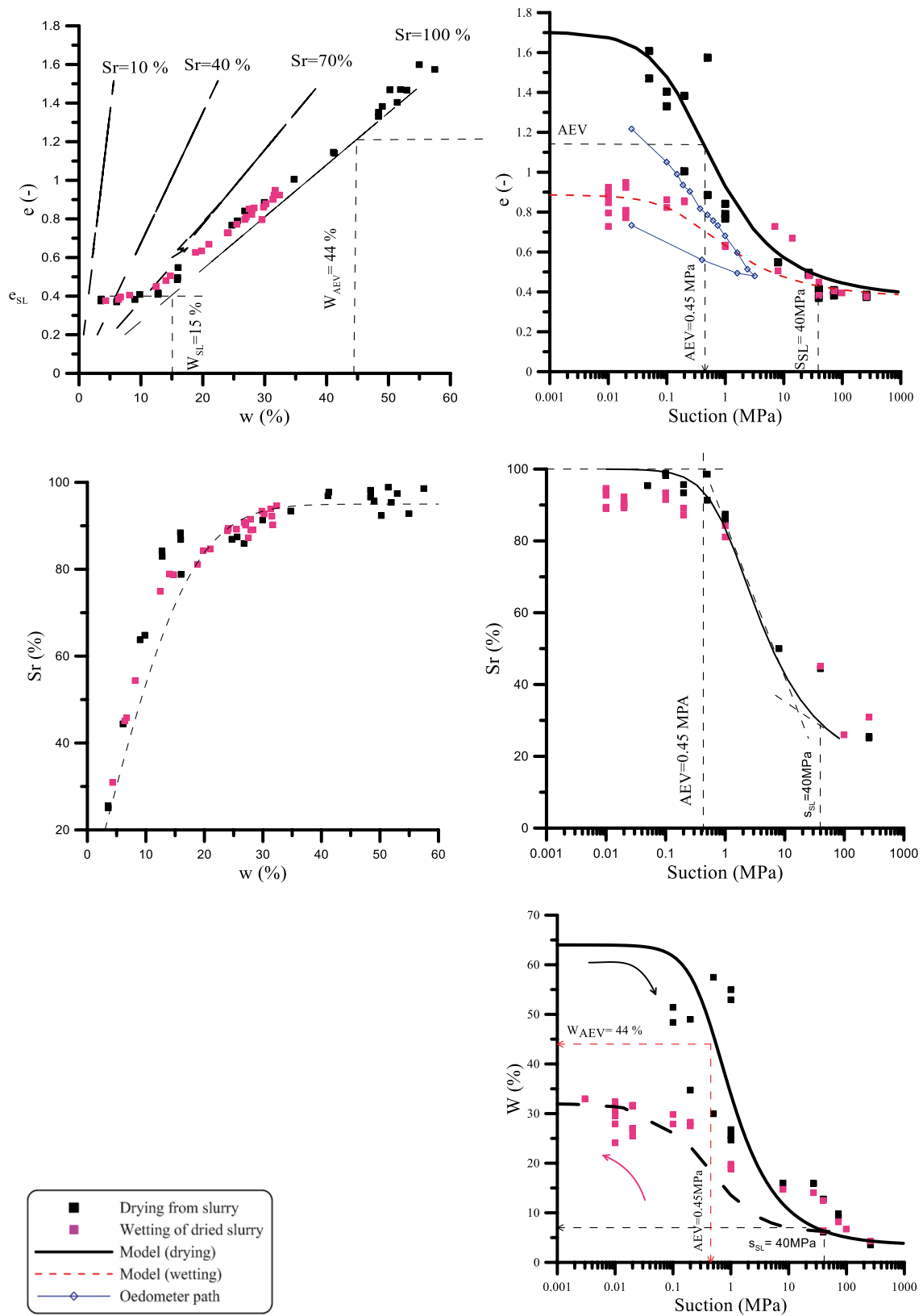
where s_s is the suction at the sample surface; s_{it_1} is the average suction at point i at time t_1 ; s_{it_2} is the average suction at point i at time t_2 ($t_2 > t_1$); and Δz is the distance between the surface and the recursive points (for example 1 and 2). To simplify the calculation, we chose a point in the middle of the sample height.

Results and discussion

Drying-wetting paths and the role of the initial state

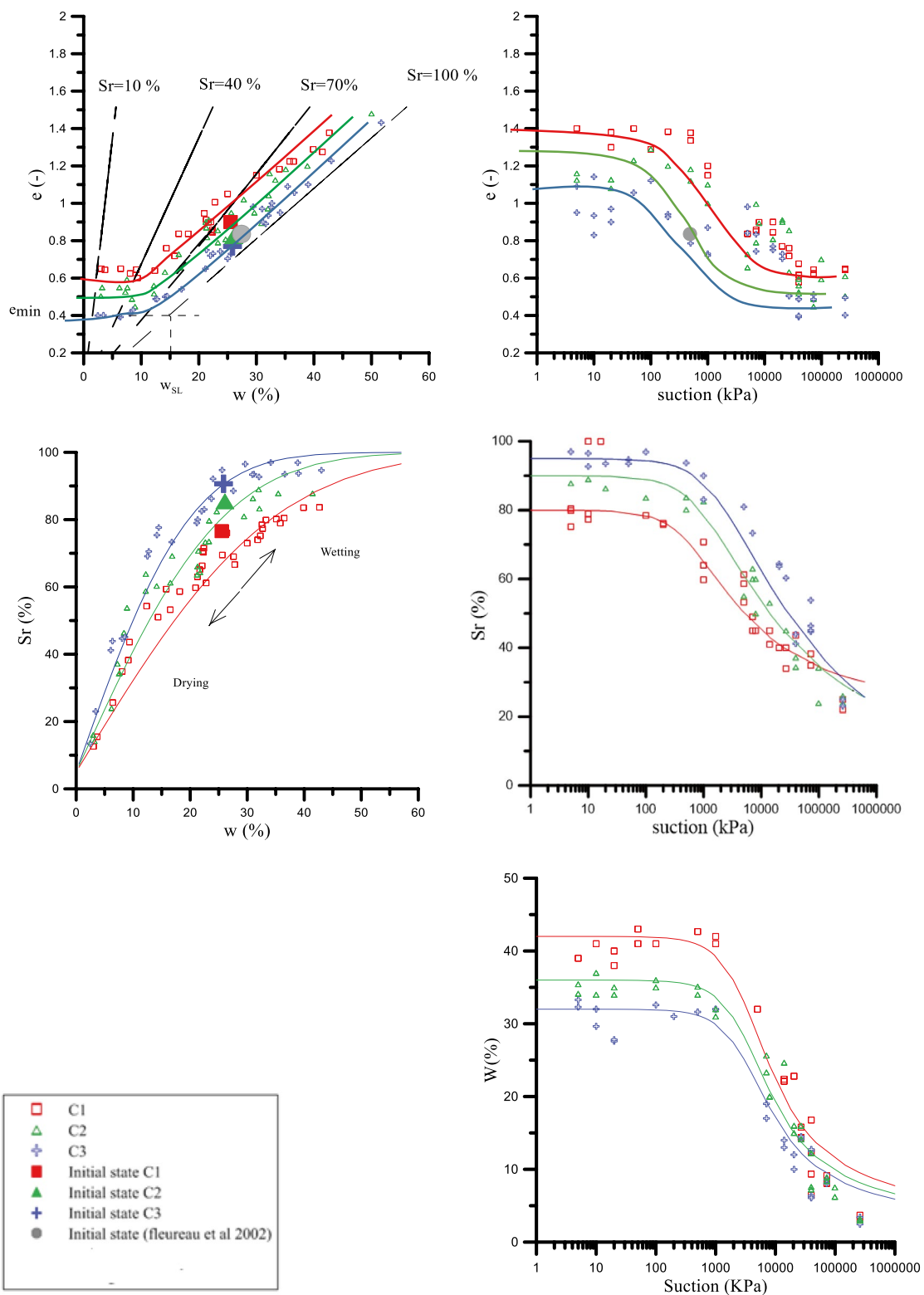
The initial value of suction for compacted materials (C1, C2, and C3) was determined by the filter paper method. When the sample is in equilibrium, the filter paper placed inside the clayey soil is extracted and the suction is measured. The sample follows a wetting path if the imposed suction is lower than the initial one. In the opposite case, the sample follows a drying path. The results of the drying–wetting paths for the sample with different initial states are shown in Fig. 3.

Figure 3a, b shows the shrinkage curves of slurry and compacted clay in the $[w, e]$ plan. On a slurry sample (Fig. 3a), the shrinkage curve follows a drying path along the saturation line of equation $e = w (\gamma_s/\gamma_w)$ until reaching the shrinkage limit, which corresponds to a water content of $w_{SL} = 15\%$ and a void ratio of $e_{SL} = 0.4$. The water content continues to decrease, and the void ratio remains constant.



(a) Slurry sample drying-wetting paths

Fig. 3 Drying-wetting paths of a slurry b compacted samples with different initial states



(b) Drying-wetting paths of compacted samples with different initial states

Fig. 3 (continued)

In the case of compacted materials (Fig. 3b), for low C1 and medium C2 compacted samples, the soil follows a wetting path from the initial state, where the void ratio increases with the water content, passing progressively from the iso-saturation line of 70% to the saturation line $S_r = 100\%$. As for the highly compacted sample (C3), being initially almost saturated, it immediately follows the saturation line. On the drying path, the void ratio decreases progressively toward the iso-saturation lines, from $S_r = 70\%$ to $S_r = 40\%$ when the shrinkage limit is reached. The water content from the shrinkage limit w_{SL} is at the intersection of the saturation line ($S_r = 100\%$) with the asymptote of the curve for $w = 0\%$.

For the slurry sample in the plan $[e, s]$ (Fig. 3a), the curve can be split into three parts. The oedometric test was superposed in this plane.

For the low suction range, below the air-entry value of about 450 kPa, the void ratio decreases according to the classical compressibility curve of a saturated soil (Fleureau et al. 1993). For the intermediate suction range, from the air-entry value to the shrinkage limit suction s_{SL} value of about 40 MPa, the suction increase leads to a decrease in the void ratio. For the high suction range (above the shrinkage limit suction s_{SL} value), the void ratio becomes almost constant.

For the compacted soils in the plan $[e, s]$ (Fig. 3b), the samples follow a drying path from their initial state (onward), when the suction is greater than the initial one. The void ratio decreases slightly until the shrinkage limit suction s_{SL} is reached, after which it remains constant. When the suction is lower than the initial one, the samples follow a wetting path with an increase in the void ratio.

Figure 3a shows that the saturation degree of a slurry sample in the $[w, S_r]$ plan decreases slowly until the air entry value (AEV) is about 450 kPa, then decreases with the water content.

For the compacted samples in the plan $[w, S_r]$, Fig. 3b, the wetting paths show that the samples do not saturate completely from their initial state. The saturation degree reaches a value between 80 and 95%, depending on the initial state of compaction. This is also illustrated in the plan $[S_r, s]$ when the suction values are about zero.

The influence of the initial state or void ratio is highlighted. The plot $[S_r, s]$ with a high void ratio is slightly lower than that with a smaller one. This result is in line with those of Romero et al. (1999) and Salager et al. (2013).

For compacted soils and when the suction is relatively low on the wetting path, the saturation degree increases to reach a maximum value below $S_r = 100\%$, which depends on the initial state of the material (Fig. 3b). The plateau of the maximum degree of saturation is reached for the suction values of 100, 150, and 250 kPa, which correspond respectively to the initial dry densities of 1.2, 1.35, and 1.5 g/cm³. The evolution of the saturation degree with suction shows that the denser the soil sample gets, the higher the suction of the resaturation value rises.

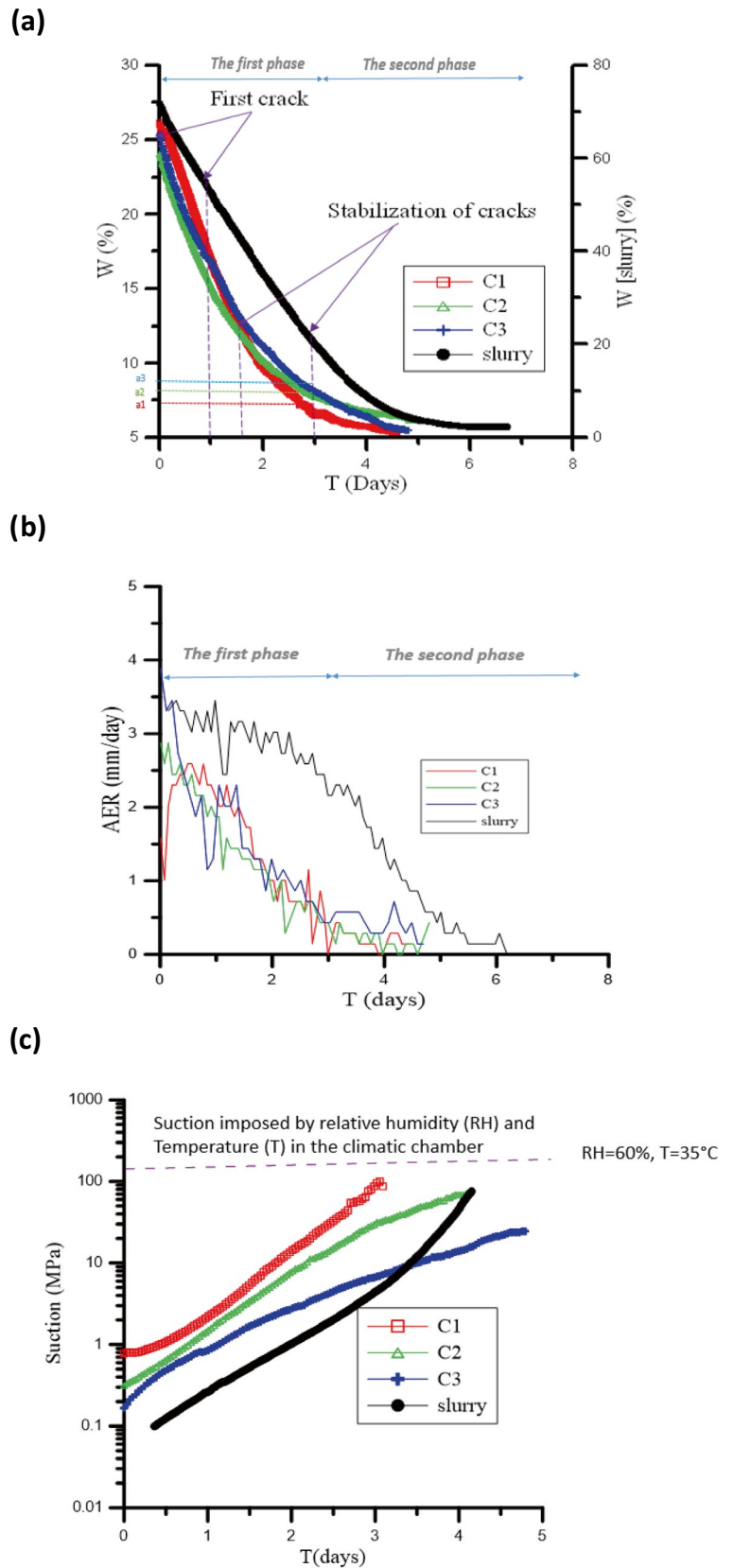
The WRC in the plan $[w, s]$ depends on the initial state; the saturated water content decreases with the increase in the soil dry density (Fig. 3). In the low suction range (below the AEV), the water content changes slowly. For the intermediate suction range (from the AEV to the suction value corresponding to the residual water content), the suction increase leads to a decrease in the water content. The water content of the various samples decreases by different magnitudes with an increase in suction. The specimen's residual points with different void ratios are almost the same. The residual water content and corresponding suction values, called residual suction values, are about 6% and 40 MPa, respectively. For the high suction range, above the residual suction value, the water content almost remains constant for the different suctions. The WRC is independent of the initial dry density when the suction is higher than 40 MPa, and the hysteresis between the drying and wetting paths is insignificant.

Evaporation parameters: the role of the initial state

Evaporation tests were performed on compacted and slurry samples with different initial states. Figure 4 shows the water content, actual evaporation rate, and suction development during desiccation.

Initially, the water content decreases linearly, then it reaches hydric equilibrium at the end of the test (Fig. 4a). In fact, the evaporated water came from two different types of voids, that is, the microvoids (microporosity) and the macrovoids (fissures or macroporosity). During the desiccation period, the rate of water loss by evaporation adheres to a linear law until reaching a stabilization of crack growth. The trend of evaporated water content against time-desiccation changes tends to reach a residual state (residual water content). This means that the crack opening kinetic is constant during the period of desiccation happening. In the second stage, the growth of cracks stopped, and only water continued to evaporate from the microporosity. Finally, the evaporation of water stopped and the moisture content reached the residual value. Note that this water content trend against time desiccation is in agreement with the results published by Yan et al. (2021). An et al. (2018) studied the role of soil texture on evaporation using clayey soil mixed with quartzite sands. The authors showed that the loss of moisture content against time follows a trend similar to the one presented in this paper, particularly for the compacted samples C1, C2, and C3. In this study, the slope of the evaporated water content-time curve is shown to be significantly affected by the microstructure of soil induced differently by compaction and slurry paths. In fact, as demonstrated by Romero et al. (1999), compaction induces a bimodal microstructure (microspores and macrospores distributions); however, drying from the slurry state induces only a mono-modal microstructure, that is, only one type of pore dominates; see, for

Fig. 4 Time evolution of various parameters: **a** water content, **b** actual evaporation rate, and **c** suction during desiccation at the middle of the sample



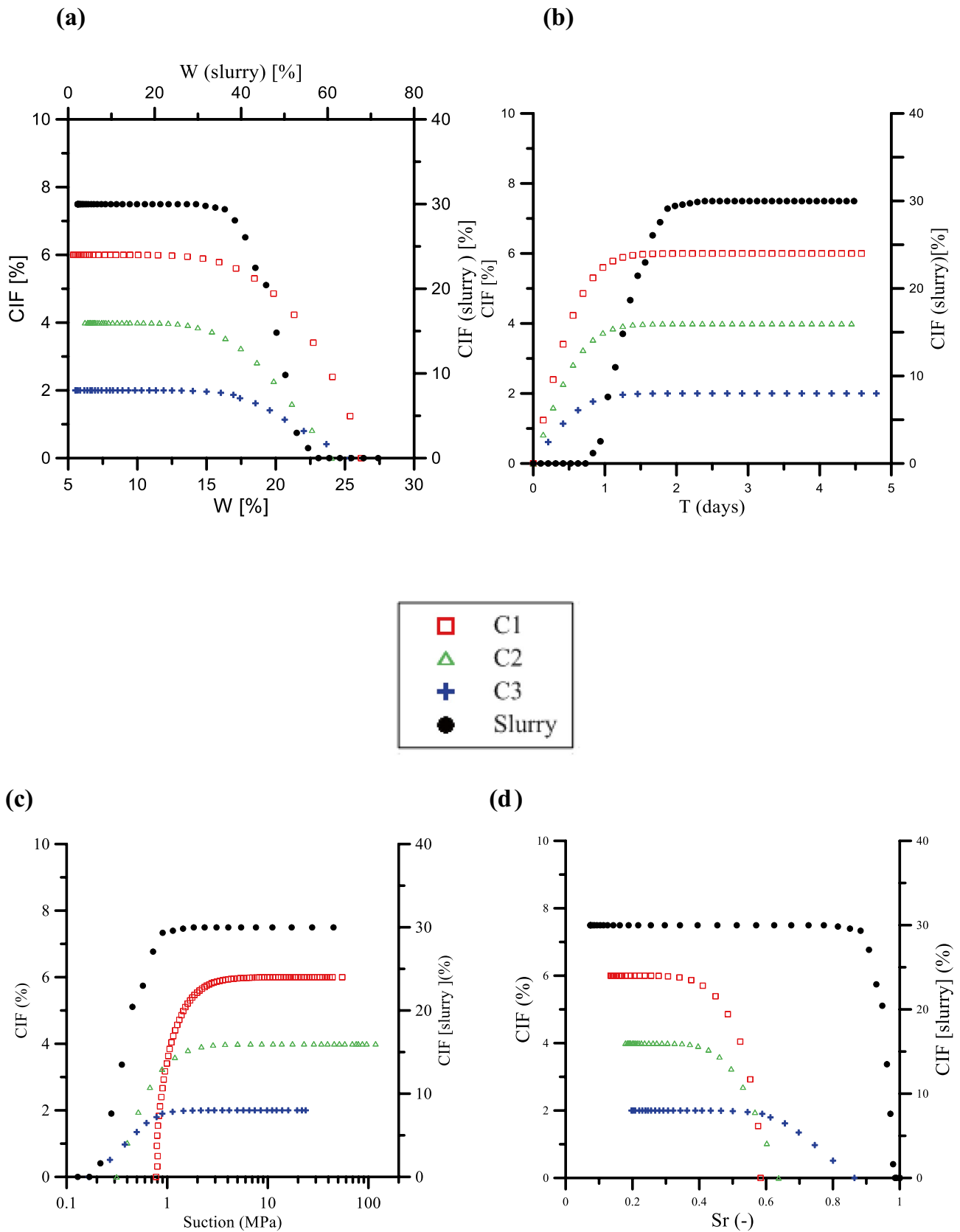


Fig. 5 Crack intensity factor variation with **a** water content, **b** time, **c** suction, and **d** saturation degree

instance, Trabelsi et al. (2018). In An et al. (2018), it was also shown that the slope of evaporated water content over time depends on the soil texture. The slope is proportional to the percentage of quartzite sand. The actual evaporation rate (AER) is related to the initial state and compaction dry density. Only two evaporation stages were identified for compacted samples, as opposed to three for a slurry sample (Fig. 4b). In fact, the higher the density, the greater the evaporated water quantity. For the slurry sample, the actual evaporation rate is almost constant during the first hours (first stage); however, this rate will continue to decrease for the compacted sample. In the second stage, the evaporation rate in the slurry clay decreases after 1 day and reaches a constant value after about 5 days. In comparison, the compacted clay takes 3 days to reach a constant evaporation value. In the last stage, the evaporation rate variation was negligible for all the samples. During desiccation, it decreases while suction increases (Fig. 4c).

Crack development

Figure 5a displays the variation of the crack ratio with water content in the plan [CIF, w]. In the beginning, the water content was ($w_i=26\%$) for the compacted samples and ($w_i=71\%$) for the slurry one, which begins drying without cracking. During desiccation, the water content decreases and the crack ratio increases after 1 h for the compacted sample and 23 h for the slurry sample. During the rest of the desiccation, the CIF stabilizes and maintains a stable value when the water content is close to the material shrinkage limit of the water content ($w_{SL}=15\%$) for the slurry samples.

For these samples, many desiccation cracks (primary and secondary cracks) are formed (Fig. 6a). However, only primary cracks developed in the compacted samples (Fig. 6b). In fact, the cracks are affected by the dry density (Fig. 5a); that is, the CIF decreases as the dry density increases.

Figure 5b shows that the CIF develops at different rates for all samples and then tends to stabilize after 2 days for the slurry soils and 1 day for the compacted ones. The same figure also demonstrates that the shrinkage limit is dependent on the initial state of the sample.

For higher densities, lumps are avoided by compaction, and mainly primary cracks develop. This may explain why the CIF values for the dense sample C3 with an initial dry density equal to 1.5 g/cm^3 are lower than those obtained for the loose sample C1 with an initial dry density of 1.2 g/cm^3 , as shown in Fig. 5a.

These observations confirm the idea that desiccation cracks develop less frequently in compacted soils with a more homogeneous porosity distribution. Thus, the heterogeneous distribution of porosity is the principal factor for the development of cracks in clayey soil. The time needed for

the cracks to propagate in the compacted clay is observed to be less than that needed by the slurry samples, which can be attributed to the stress relaxation phenomenon that occurs across the development of cracks.

Figure 5c shows that no cracks appeared in the compacted clay with different initial densities (C1, C2, and C3) when the actual suction was approximately that of resaturation (100, 150, and 200 kPa). In the case of the slurry clay, cracks appeared before reaching AEV.

Figure 5d reveals that desiccation cracks started when the saturation degree was less than 100%. In the case of the slurry sample, the first cracks appeared when the soil was almost saturated.

Figure 7 displays the evolution of CIF- T , CIF- w , CIF- s , and CIF- Sr slopes as a function of the soil's initial state, as deduced from Fig. 5, before reaching the shrinkage limit plateau.

It can be seen that the CIF- T slope is about 4 times steeper for the slurry sample than for the weakly compacted soil C1 and reaches a far higher value (about 10) for the strongly compacted soil C3 (Fig. 7a). This tendency is also observed for the slopes CIF- w (Fig. 7b), CIF- s (Fig. 7c), and CIF- Sr (Fig. 7d). These observations clearly highlight the role of the initial soil density and instantaneous hydric state (water content, suction, and saturation degree) on the magnitude of crack initiation and propagation.

Digital image correlation (DIC) analysis during the desiccation test

Figure 8 shows the displacement field in the soil during desiccation. The displacements in the center are less frequent than those at the boundaries of the sample. Besides, all the displacements are oriented toward the center. Similarly, the global shrinkage orientation in the soil sample is centripetal, which is in good agreement with Wei et al. (2021).

Figure 9 shows that the major principal strain and visible cracks are perpendicular, and their orientations are superposed on the two sides of the cracks. This confirms the idea

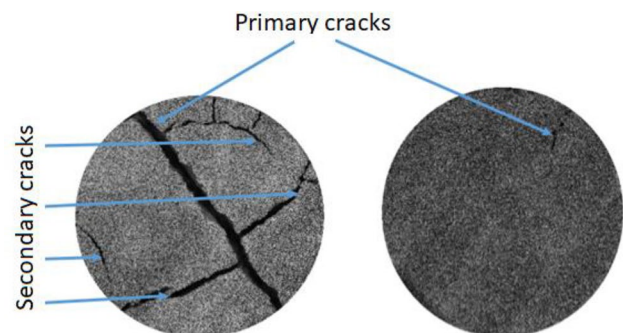


Fig. 6 The crack network in a slurry b compacted clayey soils

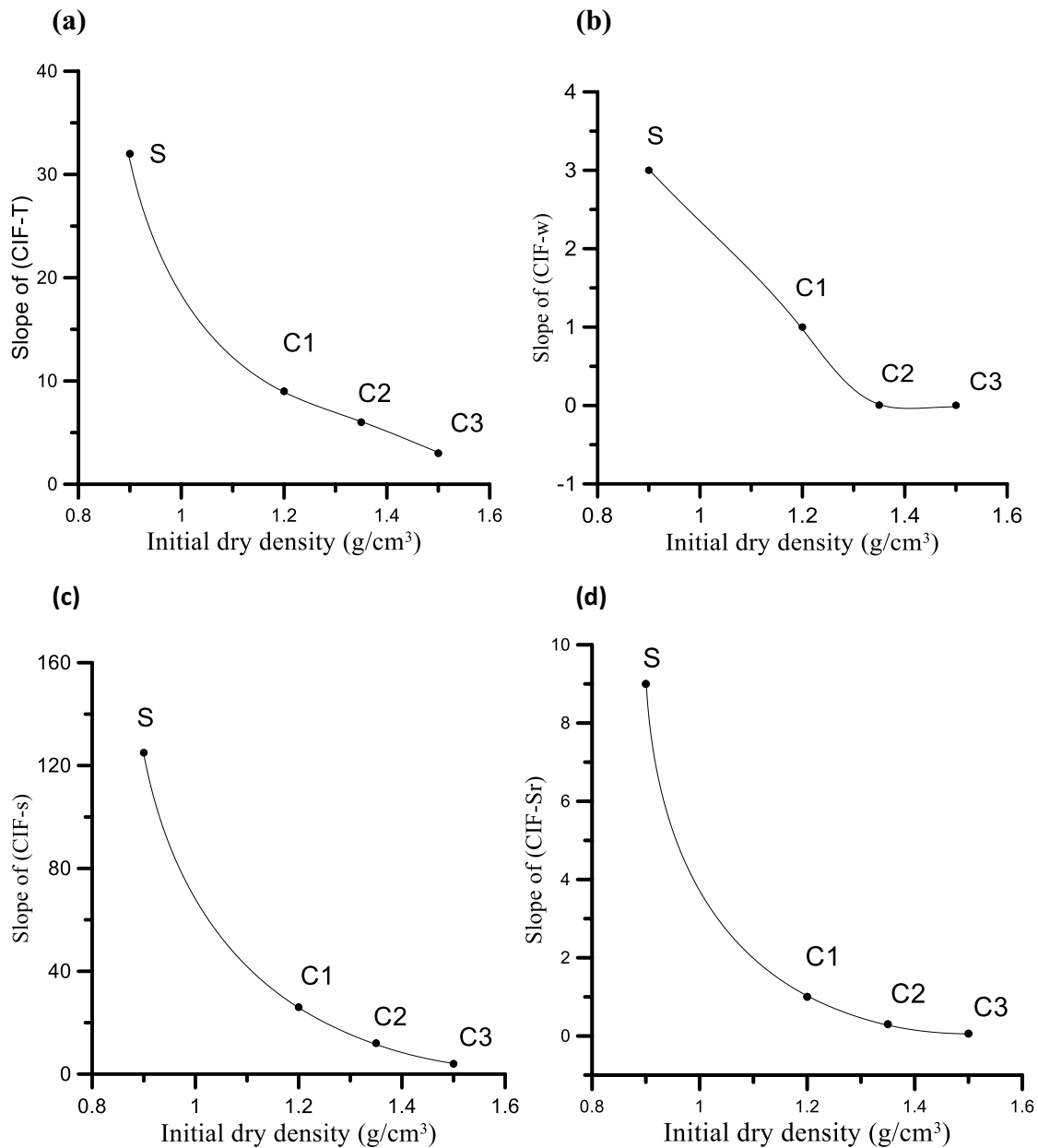


Fig. 7 Slope values of **a** [CIF, T], **b** [CIF, W], **c** [CIF, s], and **d** [CIF, Sr] of slurry (S) and compacted soils (C1, C2, and C3)

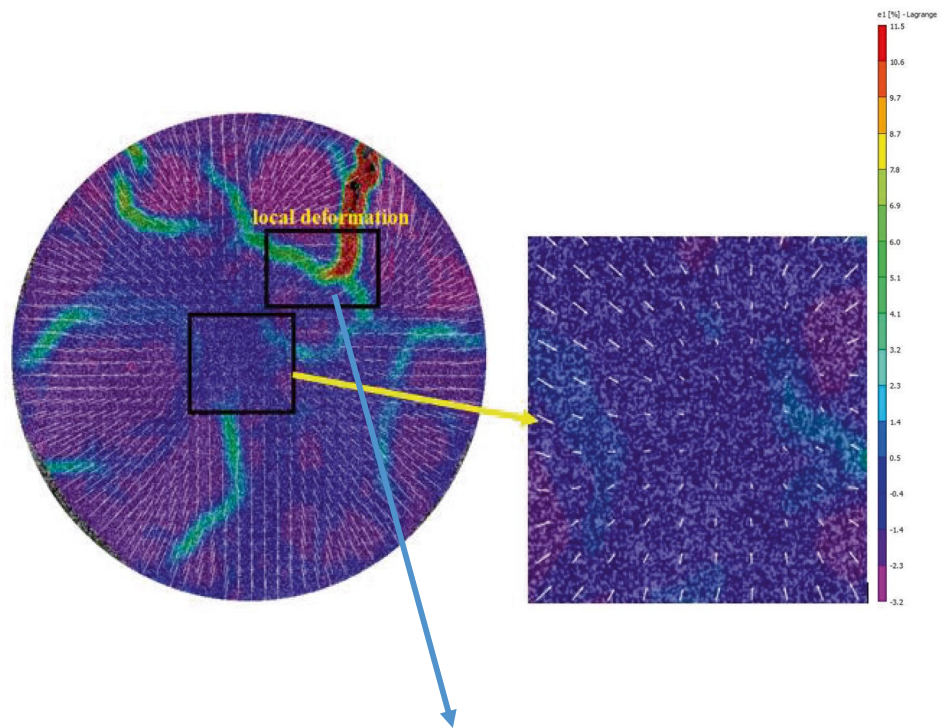
that the local deformation can be very heterogeneous during desiccation. This heterogeneity is responsible for the appearance of local tensile strain leading to desiccation cracks.

Figure 10 displays the crack pattern of the slurry sample (S) (Fig. 10a–c) and compacted clay (C3) (Fig. 10b–d), as well as their DIC analysis. Images (c) and (d) display the principal major strain map. Values vary from -3.2% (purple color) to more than $+11.5\%$ (red color). Values of zero are represented by the dark blue color. It is clear that the sample is in extension or compression when its value is positive or negative, respectively. The crack network is obvious in the slurry sample compared to the compacted one. These results correlate with the CIF variation.

Figure 11 shows the development of desiccation cracks in the compacted sample (C3) in zone 1 (see Fig. 8). At the beginning of the test, the deformations were very small, and the cracks appeared at $T=0.16$ h. The deformation becomes more important close to the cracks. The cracks propagate, and after about 1 day, they stabilize. This stabilization occurred when the water content was about $w_{sl}=15\%$.

For the slurry sample, Fig. 12 shows localization of large strains at certain locations. After 12 h, clearly visible cracks were noticeable. This network of cracks progressed and stabilized when the water content was about the shrinkage limit. This value is confirmed by the desiccation test shown and interpreted in terms of CIF (Fig. 5).

Fig. 8 Global deformation: X 300 scale



Saturated permeability

Figure 13 shows the saturated permeability evolution as a function of porosity for slurry (S) and compacted samples C1 to C3. The experimental results indicate that permeability decreases with decreasing porosity.

Rodríguez et al. (2007) suggested a saturated permeability evolution model closely tied to total porosity and expressed as follows:

$$k_{sat}(n) = k_{sat0}(b(n - n_0)) \tag{13}$$

where $k_{sat}(n)$ is the permeability coefficient corresponding to a porosity n , k_{sat0} is the saturated permeability coefficient with a reference porosity n_0 , and b is the material parameter (see Table 4). The Rodríguez model fits the experimental results for slurry and compacted samples well, and b appears to be an intrinsic parameter independent of the initial state of the material.

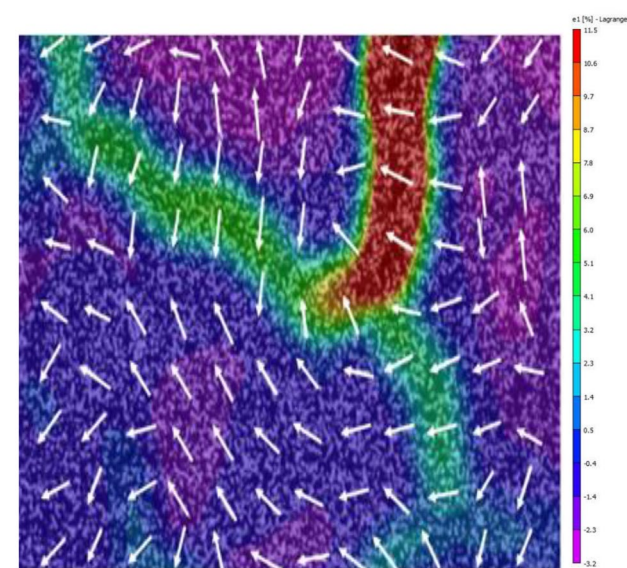


Fig. 9 Local deformation: the major principal strain

Unsaturated permeability

Figure 14a displays the actual evaporation rate (AER) variation with suction. Three stages were identified. The first is characterized by a quasi-constant evaporation and corresponds to the saturated state. The evaporation rate decreases linearly for the second stage. In this stage, the suction exceeds the AEV value ($AEV = 0.45$ MPa for the slurry sample; see Fig. 3a), and the soil is unsaturated. Therefore, the clayey soil shrinks, and cracks occur and propagate as shown in Fig. 5c. In the last stage, the material has reached the shrinkage limit ($s_{sl} = 40$ MPa), and evaporation continues at a lower rate (lower slope) without any volume change. This stage is linked to the sudden drop in the hydraulic gradient (Fig. 14b).

Figure 15 shows the unsaturated permeability variation with suction, water content, crack intensity factor, saturation degree, and soil dry density during the desiccation process.

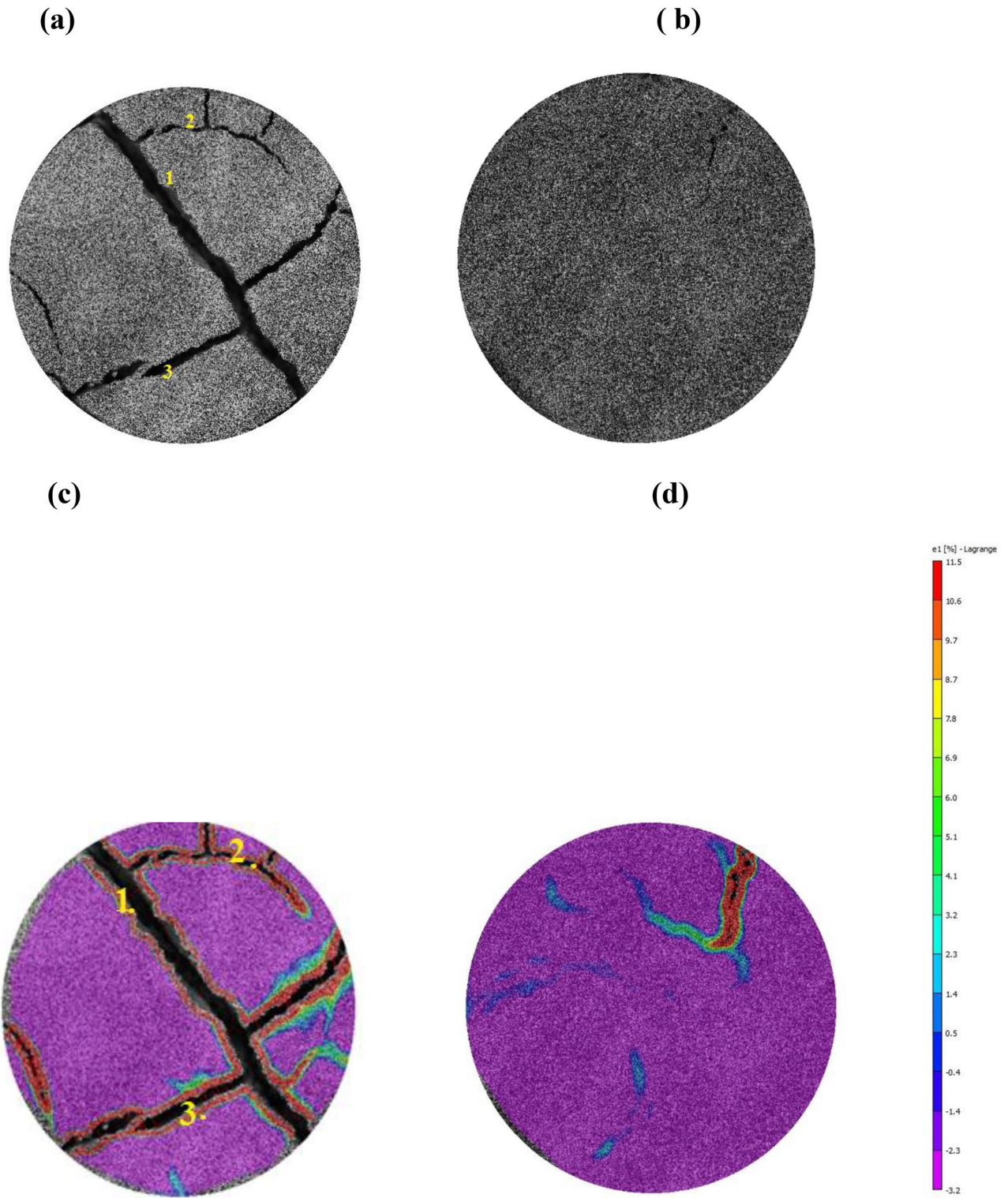
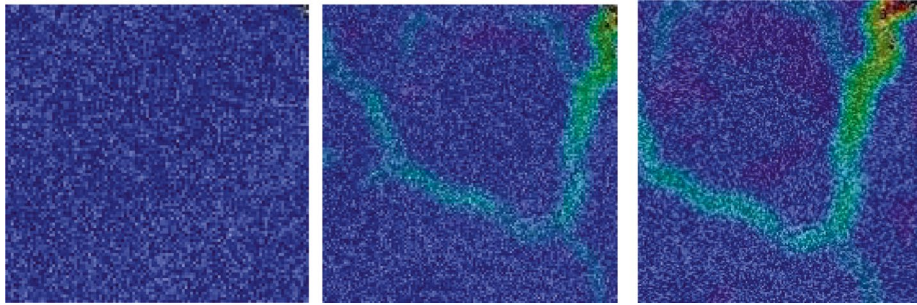
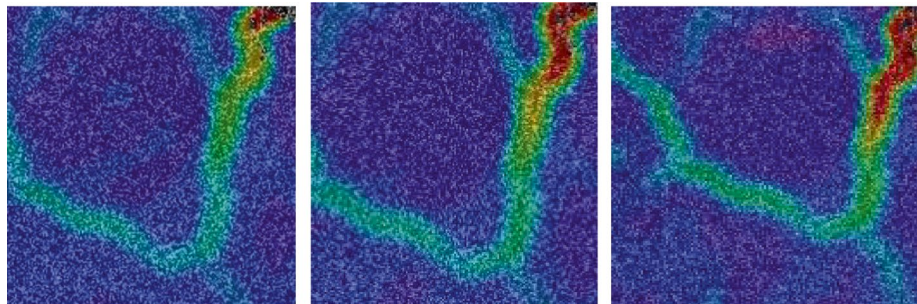


Fig. 10 Major principal strain ϵ_1 map of clayey soil at $T=2$ days for slurry and compacted samples

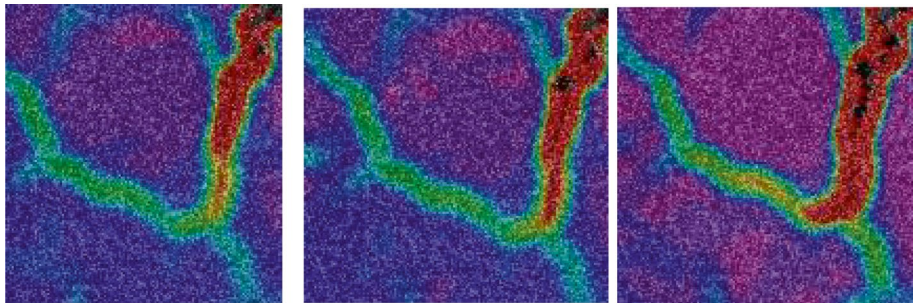
T= 0 h –W=25.5 % T=0.16 h- W=25.2% T=0.33 h- W=25.1%



T=0.5 h- W=25.0% T=0.66 h- W=24.8% T=0.8h-W=24.5 %



T= 1.8 h –W=24.3 % T=2.8 h- W=23.8 % T=28 h-W=15.3 %



T= 39 h –W=12.5 % T=50 h- W=10.8% T=100h-W=6.1 %

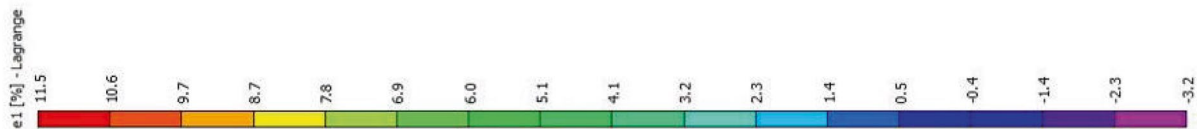
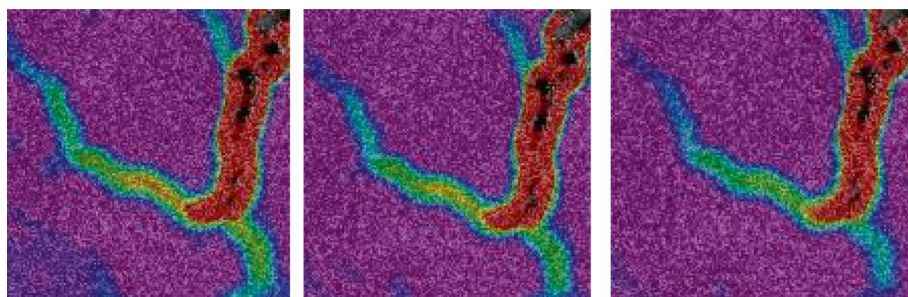


Fig. 11 Principle major strain distribution during drying around a single crack in compacted clay C3 with an initial dry density of 1.5 g/cm.³

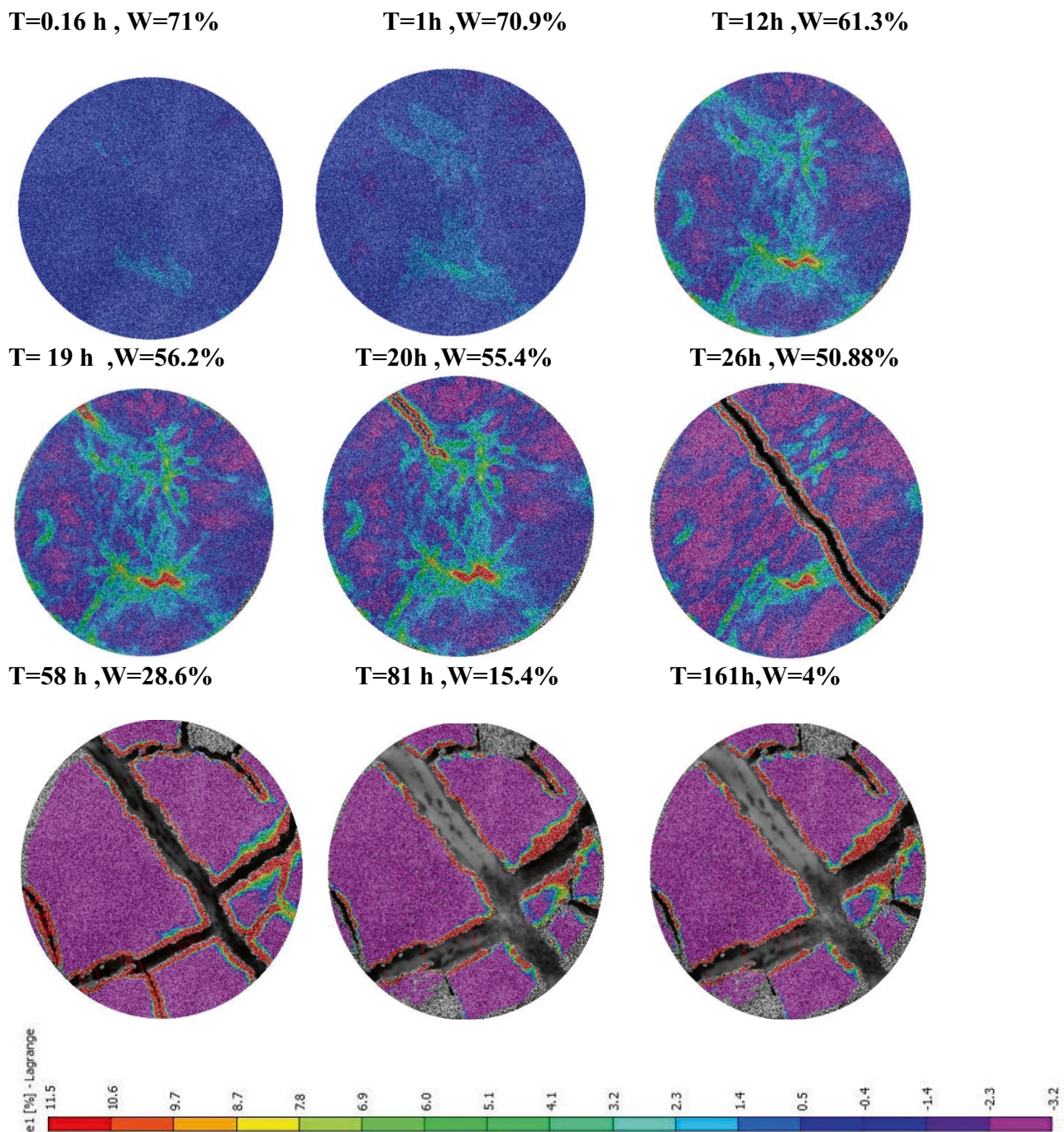


Fig. 12 Strain field evolution versus time for slurry samples

Permeability evolved in two phases: the first occurred during the desiccation process before the shrinkage limit was reached, and the second took place after the shrinkage limit was reached.

During desiccation, the soil shrank, and the cracks appeared and grew. After that, permeability decreased until it reached the shrinkage limit, and then it became governed by the desiccation cracks. It should be noted here that since

the unsaturated permeability is a 3D parameter including the vertical dimension, the dependency function between permeability and cracks needs to be more quantified when the 3D crack network is quantified. So far, the CIF has been characterized by ImageJ calculations based on the upper area of the sample.

On the other hand, when the suction of samples (S, C1, C2, and C3) increased during desiccation, their unsaturated

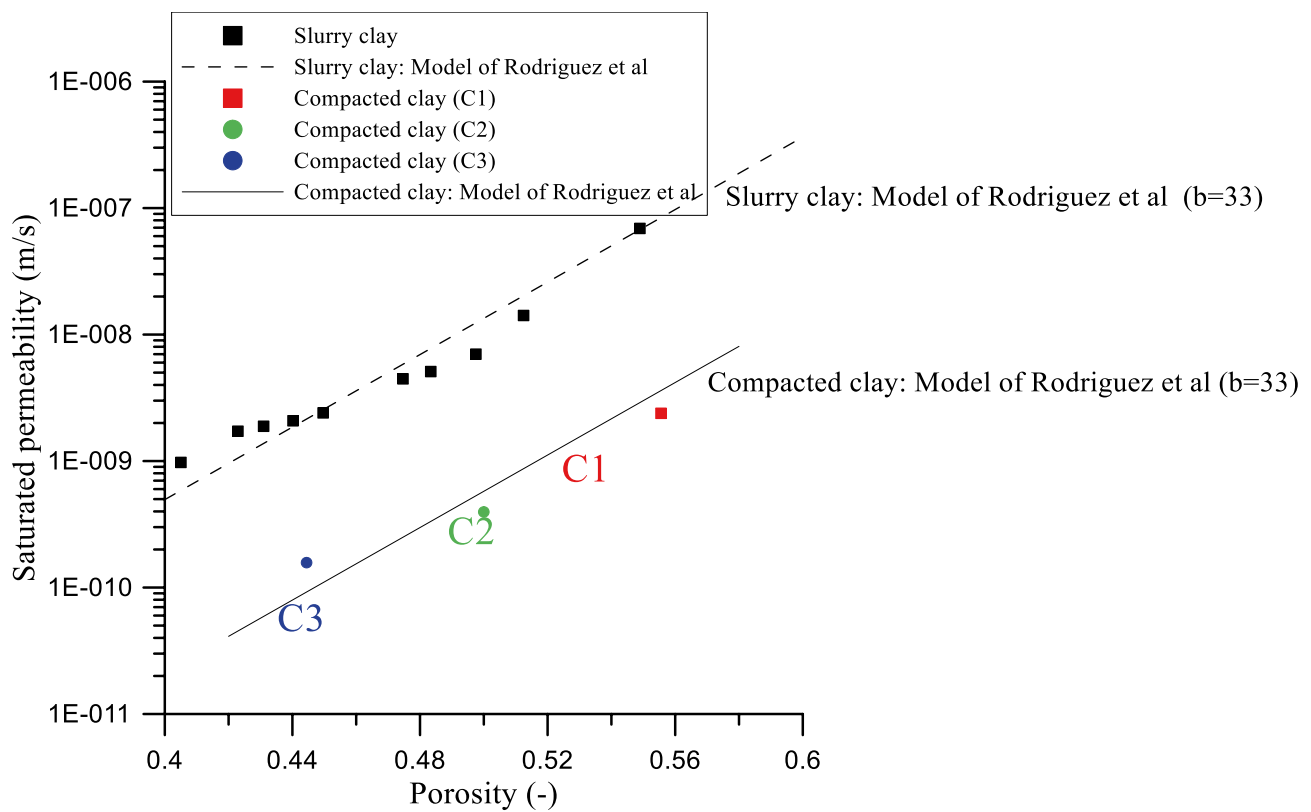


Fig. 13 Comparison between predicted and measured saturated hydraulic conductivity with porosity

permeability decreased (Fig. 15a), along with the decrease of the water content (Fig. 15b) and the increase of CIF (Fig. 15c). The sample shrank and caused a decrease in the unsaturated permeability and an increase in the soil matrix density (Fig. 15d). With the decrease in the saturation degree below $Sr=100\%$, the unsaturated permeability decreased because of densification (Fig. 15e).

At the end of the desiccation test, the unsaturated permeability increased rapidly, especially for the loose samples (S, C1) (see Fig. 16a) compared to the dense sample C3 (Fig. 16b).

Physically, this may be linked to the increase in desiccation cracks in loose samples (S and C1). In fact, the specimen reaches the shrinkage limits ($w_{SL}=15\%$, $s_{sl}=40$ MPa), beyond which there are no further volume changes (Fig. 15). Then, the cracks can directly affect the unsaturated permeability.

As already stated or known, the unsaturated permeability depends on the initial density and pore structure. Therefore, the

increase in the dry density induces changes in the micropore size distribution and affects the ability of the soil to shrink and permit water passage under unsaturated conditions.

Figure 16 shows a decrease in the matrix porosity upon drying due to shrinkage and an increase in the macro porosity due to cracks. In fact, during drying, a densification process is noticed at the microscopic level, but an evolution of desiccation cracks occurs also at the macroscopic level, leading to an increase in cracks and causing an increase in permeability.

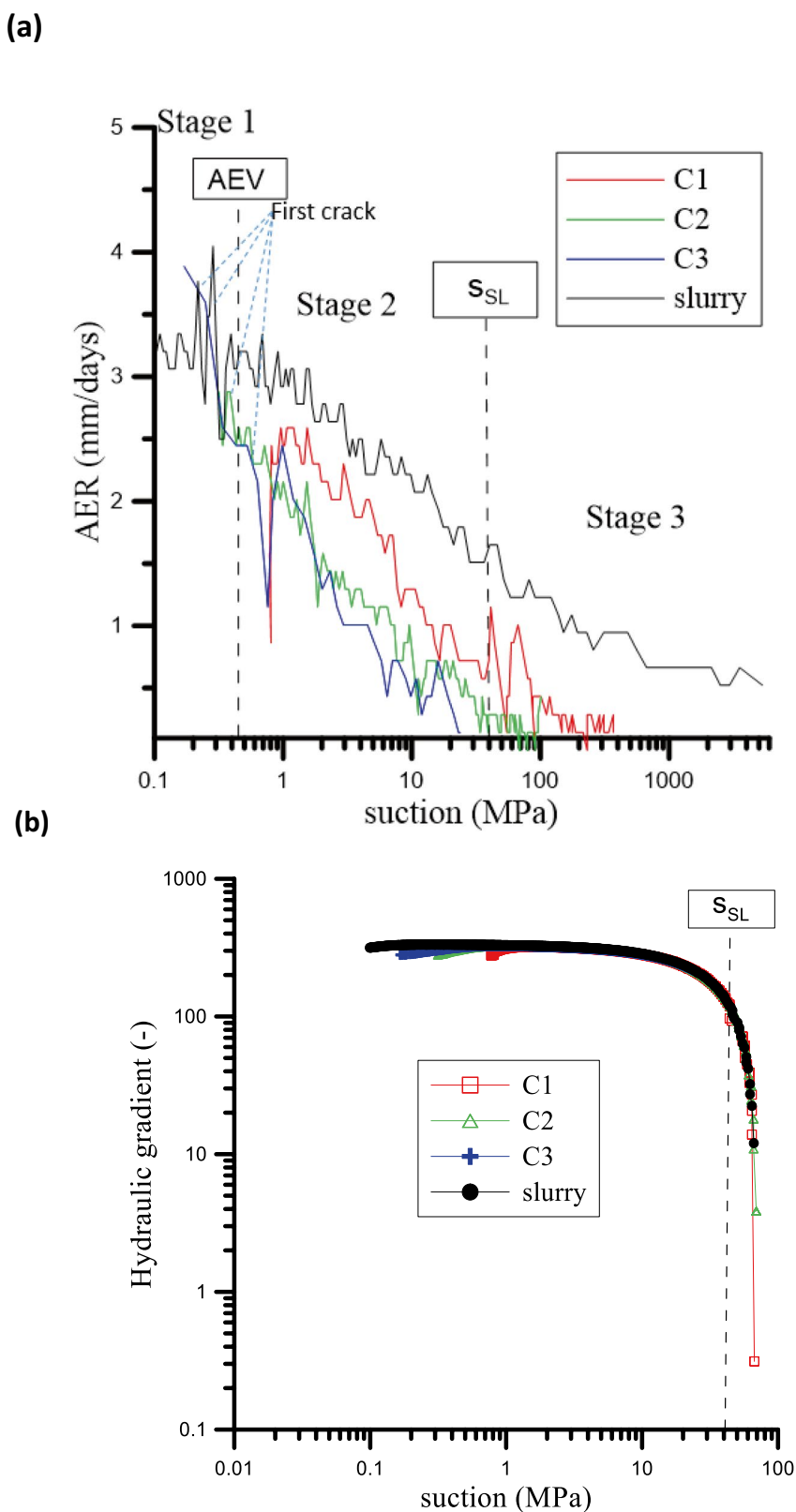
Unlike the CIF value of the compacted sample (only 4% for C2), the CIF of the slurry sample (S) is more important at 30% (Fig. 15c and Fig. 17). As for densification, it amounts to almost 40% for the slurry soil compared to the figure of 18% for the compacted sample C2 (Fig. 17). In the case of the slurry sample (Fig. 16a), the homogeneous shrinkage causes the densification of material, which decreases permeability, whereas the appearance of cracks increases permeability. These two phenomena occur simultaneously; they compensate for each other, and permeability becomes almost constant as a function of Sr (Fig. 15e).

Figure 17 displays the CIF variation versus the matrix density for both the slurry and compacted samples. The desiccation causes shrinkage in the solid matrix, which results in clayey soil densification and a decrease in

Table 4 Eq. 8 parameters

Parameters	C1	C2	C3	S
k_{sat0} (m/s)	3 E -9	3 E -9	3 E -9	7 E -8
b	33	33	33	33
n_0	0.55	0.55	0.55	0.55

Fig. 14 Variation of **a** evaporation rate **b** hydraulic gradient



permeability. On the other hand, drying also causes the appearance of cracks, causing an increase in the total porosity and, consequently, an increase in the soil permeability.

Based on all these results, it is concluded that the new experimental setup is suitable for the determination of permeability in cracked clay under various initial conditions.

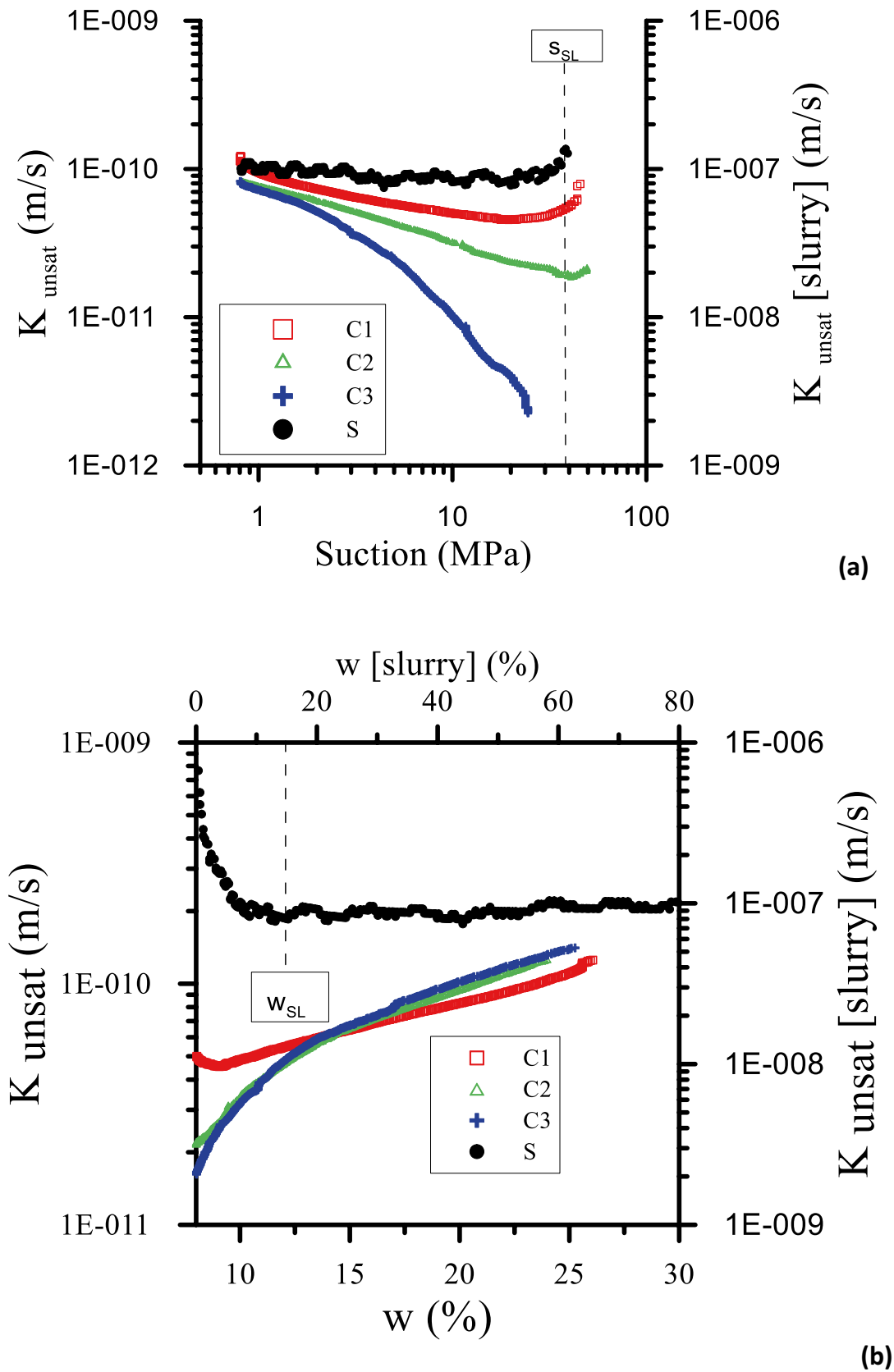


Fig. 15 Unsaturated permeability variation versus a suction, b water content, c CIF, d dry density, and e saturation degree during evaporation test

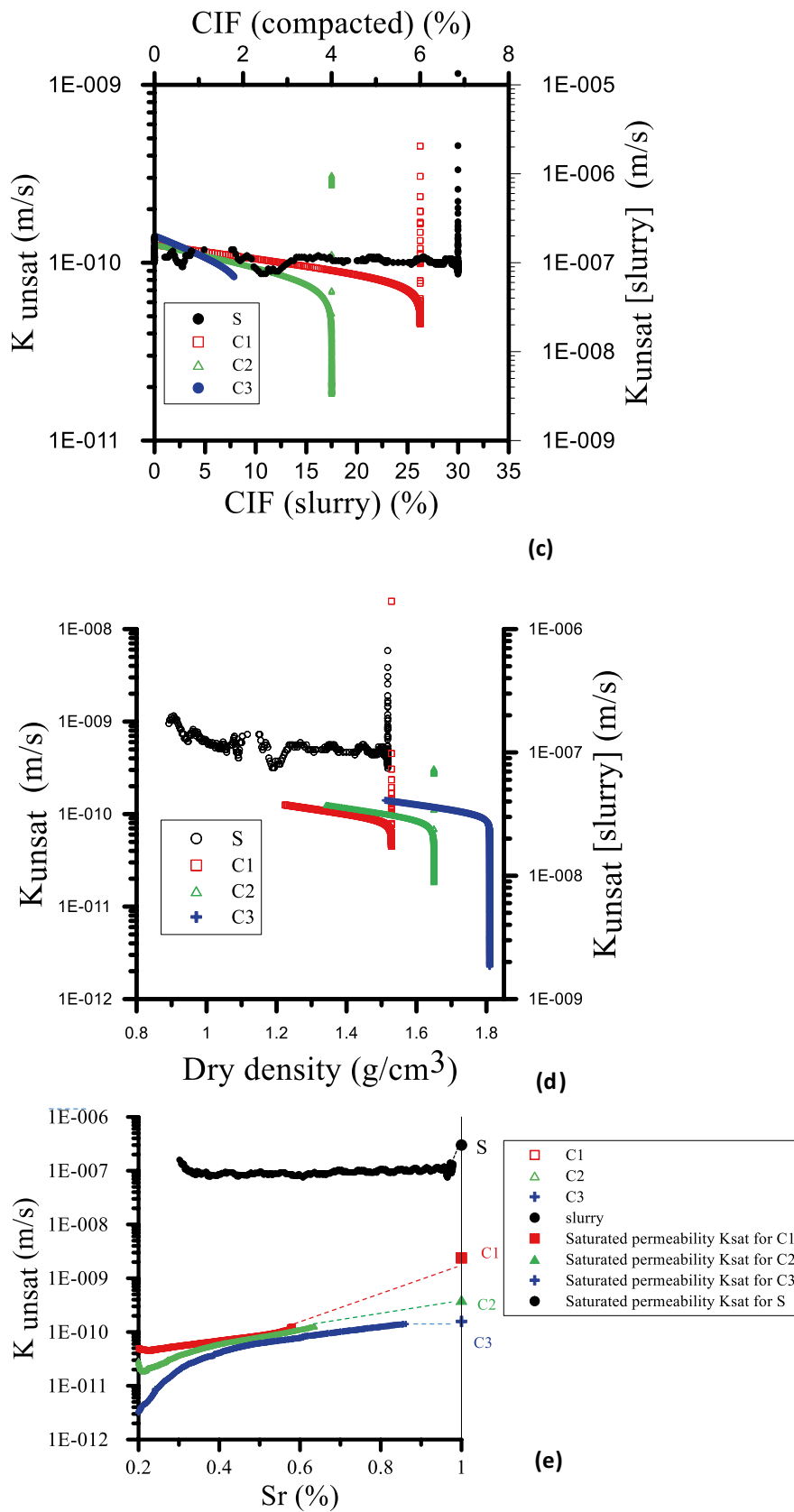


Fig. 15 (continued)

Fig. 16 Slurry and compacted sample structural analysis at the end of drying **a** for slurry sample S **b** for compacted sample C3

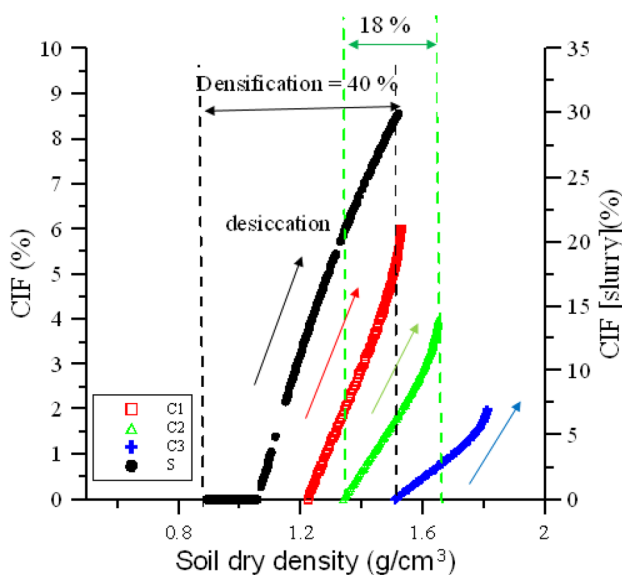
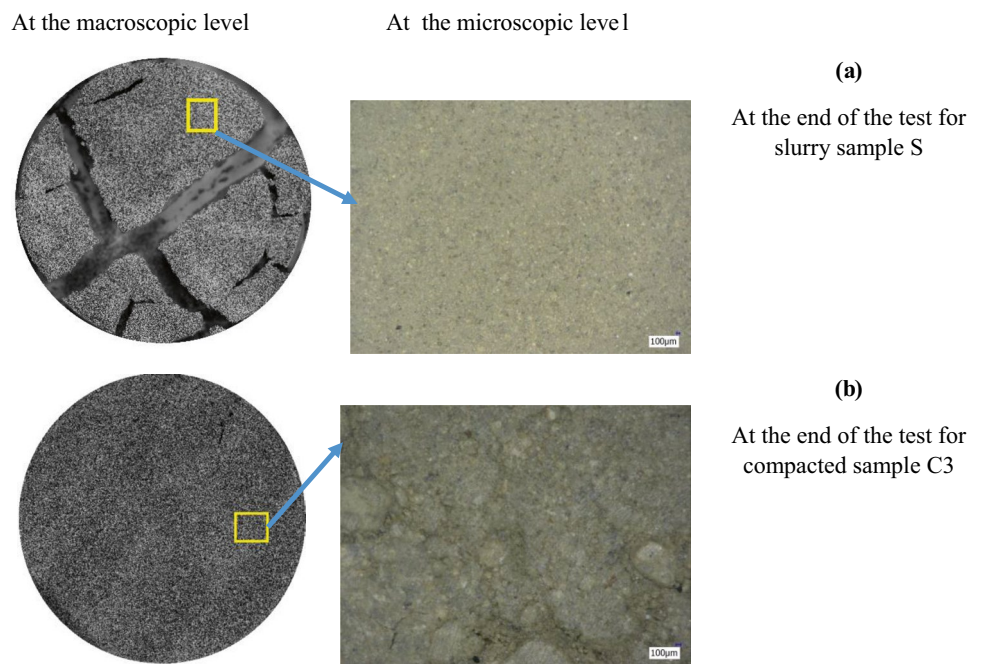


Fig. 17 Variation of density with crack intensity factor during drying test

Conclusion

The unsaturated permeability during desiccation of the clayey soil was investigated based on the water retention curve (WRC), actual evaporation rate (AER) as well as cracking, and microstructure and macrostructure evolutions. The effects of suction, initial density, volume change, and desiccation-induced cracking led to the following conclusions:

- Micro- and macrostructural changes affect the saturated and unsaturated permeabilities during desiccation. The macrostructural changes take place because of desiccation cracks, while the microstructural changes occur due to shrinkage and densification of the soil matrix.
- In the desiccation shrinkage test, the combined use of DIC and image analysis techniques allows for characterizing the strain fields before, during, and after crack initiation and propagation and highlighting local tensile stress concentrations, which are at the origin of the initiation of cracks.
- The crack intensity factor (CIF) depends on the instantaneous hydric state (suction, water content, and saturation degree). On the other hand, the slopes of the CIF-hydric state relationships decrease with the increase of the initial density.
- A new method, derived from the IPM technique, was developed. Then, the unsaturated permeability can be simply and quickly measured without using complex proximity sensors.
- During desiccation and before the initiation of cracks, the unsaturated permeability decreases with the decrease in water content, and the dry density increases due to shrinkage.
- After the initiation of cracking and before reaching the shrinkage limit, two simultaneous and contradictory phenomena occur: the crack network tends to increase permeability while the shrinkage of the soil matrix continues, resulting in its densification and decrease in permeability.
- When the shrinkage limit is reached, there is no volume change in the soil matrix. The unsaturated permeability increases sharply due to the crack network, in particular

for initially loose soils (slurry S and weakly compacted soil C1).

Funding The authors extend their appreciation to the deputyship for research and innovation, Ministry of Education in Saudi Arabia for funding this research work through the project number “IF_2020-NBU_459”.

Availability of data and material The datasets used and/or analyzed during the current study are available from the corresponding author on reasonable request.

Declarations

Conflict of interest The authors declare no competing interests.

References

- An N, Tang CS, Xu SK, Gong XP, Shi B, Inyang HI (2018) Effects of soil characteristics on moisture evaporation. *Eng Geol* 239:126–135. <https://doi.org/10.1016/j.enggeo.2018.03.028>
- Birle E, Heyer D, Vogt N (2008) Influence of the initial water content and dry density on the soil–water retention curve and the shrinkage behavior of a compacted clay. *Acta Geotech* 3(3):191–200
- Blackwell PS, Graham JP, Armstrong JV, Ward MA, Howse KR, Dawson CJ, Butler AR (1986) Compaction of a silt loam soil by wheeled agricultural vehicles. I. Effects upon soil conditions. *Soil Tillage Res* 7(1–2):97–116
- Cheng Q, Tang CS, Zeng H, Zhu C, An N, Shi B (2020) Effects of microstructure on desiccation cracking of a compacted soil. *Eng Geol* 265:105418. <https://doi.org/10.1016/j.enggeo.2019.105418>
- Costa S, Kodikara J, Thusyanthan NI (2008) Study of desiccation crack evolution using image analysis. *Unsaturated Soils Adv Geo-Eng* pp 175–180
- Costa S, Kodikara JK, Shannon B (2013) Salient factors controlling desiccation cracking of clay in laboratory experiments. *Géotechnique* 63(1):18–29
- Delage P, Howat MD, Cui YJ (1998) The relationship between suction and swelling properties in a heavily compacted unsaturated clay. *Eng Geol* 50(1–2):31–48
- El Hajjar A, Ouahbi T, Eid J, Hattab M, Taibi S (2020) Shrinkage cracking of unsaturated fine soils: new experimental device and measurement techniques. *Strain*. John Wiley & Sons Ltd. <https://doi.org/10.1111/str.12352>
- El Hajjar A, Ouahbi T, Taibi S, Eid J, Hattab M, Fleureau JM (2021) Assessing crack initiation and propagation in flax fiber reinforced clay subjected to desiccation. *Constr Build Mater*. <https://doi.org/10.1016/j.conbuildmat.2021.122392>
- Eid J, Taibi S, Fleureau JM, Hattab M (2015) Drying, cracks and shrinkage evolution of a natural silt intended for a new earth building material. Impact of reinforcement. *Constr Build Mater* 86:120–132
- Fleureau JM, Kheirbek-Saoud S, Soemitro R, Taibi S (1993) Behavior of clayey soils on drying–wetting paths. *Can Geotech J* 30(2):287–296
- Fujimaki H, Inoue M (2003) A flux-controlled steady-state evaporation method for determining unsaturated hydraulic conductivity at low matric pressure head values. *Soil Sci* 168(6):385–395
- Gueddouda MK et al (2016) Hydraulic properties of dune sand–bentonite mixtures of insulation barriers for hazardous waste facilities. *Journal of Rock Mechanics and Geotechnical Engineering* 8(4):541–550
- Groisman A, Kaplan E (1994) An experimental study of cracking induced by desiccation. *Europhys Lett* 25(6):415–420
- Hallett PD, Newson TA (2001) A simple fracture mechanics approach for assessing ductile crack growth in soil. *Soil Sci Soc Am J* 65(4):1083–1088
- Hattab M, Taibi S, Fleureau JM (2020) Mud shrinkage and cracking phenomenon experimental identification using digital image correlation. *Dynamics, Strength of Materials and Durability in Multiscale Mechanics* pp 379–403
- Horn R, Domzwał H, Słowińska-Jurkiewicz A, Van Ouwerkerk C (1995) Soil compaction processes and their effects on the structure of arable soils and the environment. *Soil and Tillage Research* 35(1–2):23–36
- Julina M, Thyagaraj T (2019) Quantification of desiccation cracks using X-ray tomography for tracing shrinkage path of compacted expansive soil. *Acta Geotech* 14(1):35–56
- Julina M, Thyagaraj T (2020) Combined effects of wet-dry cycles and interacting fluid on desiccation cracks and hydraulic conductivity of compacted clay. *Eng Geol* 267:105505. <https://doi.org/10.1016/j.enggeo.2020.105505>
- Lakshminantha MR, Prat PC, Ledesma A (2009) Image analysis for the quantification of a developing crack network on a drying soil. *Geotech Test J* 32(6):505–515
- Li P, Shao S, Xiao T, Zhu D (2021) Pore-size distribution evolution of intact, compacted, and saturated loess from China during consolidation and shearing. *Adv Civil Eng*. <https://doi.org/10.1155/2021/6644471>
- Louati F, Mabrouk A, Trabelsi H, Jamei M, Zenzri H (2021) Flow exchange and unsaturated permeability of cracked clay: experimental and modelling. *Eur J Environ Civil Eng* 1–17. <https://doi.org/10.1080/19648189.2021.1989051>
- Louati F, Trabelsi H, Jamei M, Taibi S (2018a) Impact of wetting–drying cycles and cracks on the permeability of compacted clayey soil. *Eur J Environ Civil Eng* 1–26. <https://doi.org/10.1080/19648189.2018.1541144>
- Louati F, Houcem T, Jamei M (2018b) Unsaturated permeability prediction using natural evaporation method in cracked clay. *Proceedings of the 7th International Conference on Unsaturated Soils*, Hong Kong, China. <https://www.issmge.org/publications/online-library>. Accessed 7 August.
- Marinho FA (2005) Nature of soil–water characteristic curve for plastic soils. *Journal of Geotechnical and Geoenvironmental Engineering* 131(5):654–661
- McNabb DH, Startsev AD, Nguyen H (2001) Soil wetness and traffic level effects on bulk density and air-filled porosity of compacted boreal forest soils. *Soil Sci Soc Am J* 65(4):1238–1247
- Miller CJ, Yesiller N, Yaldo K, Merayyan S (2003) Closure to “impact of soil type and compaction conditions on soil water characteristic” by CJ Miller, N. Yesiller, K. Yaldo, and S. Merayyan. *J Geotech Geoenviron Eng* 129(12):1169–1170
- Peron H, Hueckel T, Laloui L, Hu L (2009) Fundamentals of desiccation cracking of fine-grained soils: experimental characterisation and mechanisms identification. *Can Geotech J* 46:1177–1201
- Rodríguez R, Sanchez M, Ledesma A, Lloret A (2007) Experimental and numerical analysis of desiccation of a mining waste. *Can Geotech J* 44(6):644–658
- Romero E, Gens A, Lloret A (1999) Water permeability, water retention and microstructure of unsaturated compacted Boom clay. *Eng Geol* 54(1–2):117–127
- Romero E, Gens A, Lloret A (2001) Temperature effects on the hydraulic behaviour of an unsaturated clay. *Unsaturated soil concepts and their application in geotechnical practice*. Springer, Dordrecht, pp 311–332
- Salager S, Nuth M, Ferrari A, Laloui L (2013) Investigation into water retention behaviour of deformable soils. *Can Geotech J* 50(2):200–208

- Schindler U, Doerner J, Mueller L (2015) Simplified method for quantifying the hydraulic properties of shrinking soils. *J Plant Nutr Soil Sci* 178(1):136–145
- Sun DA, Sheng D, Xu Y (2007) Collapse behaviour of unsaturated compacted soil with different initial densities. *Can Geotech J* 44(6):673–686
- Sun DA, You G, Annan Z, Daichao S (2016) Soil–water retention curves and microstructures of undisturbed and compacted Guilin lateritic clay. *Bull Eng Geol Env* 75(2):781–791
- Tang C, Shi B, Liu C, Zhao L, Wang B (2008) Influencing factors of geometrical structure of surface shrinkage cracks in clayey soils. *Eng Geol* 101(3–4):204–217
- Tang CS, Cui YJ, Shi B, Tang AM, Liu C (2011) Desiccation and cracking behaviour of clay layer from slurry state under wetting–drying cycles. *Geoderma* 166(1):111–118
- Tessier D (1975) Recherches expérimentales sur l'organisation des particules dans les argiles. Application à l'étude de 4 pâtes argileuses "calciques" en voie de dessiccation (Doctoral dissertation, l'auteur)
- Trabelsi H, Jamei M, Zenzri H, Olivella S (2012) Crack patterns in clayey soils: Experiments and modeling. *Int J Numer Anal Meth Geomech* 36(11):1410–1433
- Trabelsi H, Romero E, Jamei M (2018) Tensile strength during drying of remoulded and compacted clay: The role of fabric and water retention. *Appl Clay Sci* 162:57–68. <https://doi.org/10.1016/j.clay.2018.05.032>
- Vanapalli SK, Fredlund DG, Pufahl DE (1999) The influence of soil structure and stress history on the soil–water characteristics of a compacted till. *Geotechnique* 49(2):143–159
- Wang JD, Li P, Ma Y, Vanapalli SK (2019) Evolution of pore-size distribution of intact loess and remolded loess due to consolidation. *J Soils Sediments* 19(3):1226–1238
- Wang Y, Feng Di, Ng CWW (2013) Modeling the 3D crack network and anisotropic permeability of saturated cracked soil. *Comput Geotech* 52:Pages 63–70
- Wei X, Bicalho K, El Hajjar A, Taibi S, Hattab M, Fleureau J (2020) Experimental techniques for the study of the cracking mechanisms in drying clays. *Geotech Test J* 2:323–338. <https://doi.org/10.1520/GTJ20190430>
- Wei X, Hattab M, Taibi S, Bicalho KV, Xu L, Fleureau JM (2021) Crack development and coalescence process in drying clayey loess. *Geomech Eng* 25(6):535–552
- Williams J, Shaykewich CF (1969) An evaluation of polyethylene glycol (PEG) 6000 and PEG 20,000 in the osmotic control of soil water matric potential. *Can J Soil Sci* 49(3):397–401
- Xu P, Zhang Q, Qian H, Qu W, Li M (2020) Microstructure and permeability evolution of remolded loess with different dry densities under saturated seepage. *Eng Geol* 282:105875. <https://doi.org/10.1016/j.enggeo.2020.105875>
- Yan C, Zheng Y, Ke W, Wang G (2021) A FDEM 3D moisture migration–fracture model for simulation of soil shrinkage and desiccation cracking. *Comput Geotech* 140. <https://doi.org/10.1016/j.compgeo.2021.104425>
- Zhou AN, Sheng D, Li J (2014) Modelling water retention and volume change behaviours of unsaturated soils in nonisothermal conditions. *Comput Geotech* 55:1–13

Springer Nature or its licensor (e.g. a society or other partner) holds exclusive rights to this article under a publishing agreement with the author(s) or other rightsholder(s); author self-archiving of the accepted manuscript version of this article is solely governed by the terms of such publishing agreement and applicable law.